Contents lists available at ScienceDirect

Sustainable Chemistry for the Environment

journal homepage: www.editorialmanager.com/scenv

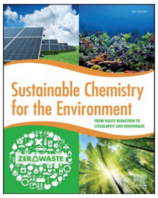

Facile preparation of triangular-like polycrystalline ceria as supporting carrier in catalysis exemplified by Ni/CeO_2 catalyzed oxidation and hydrogenation reactions

Sofia Stefa [a,b], Maria Lykaki [a], Georgios Varvoutis [c], Maria Zografaki [b,d], Vassilios D. Binas [b,d], George E. Marnellos [e,f], Michalis Konsolakis [a,*]

[a] *School of Production Engineering and Management, Technical University of Crete, Chania, Greece*
[b] *Institute of Electronic Structure and Laser, Foundation for Research and Technology, Heraklion, Greece*
[c] *Department of Mechanical Engineering, University of Western Macedonia, Kozani, Greece*
[d] *School of Chemistry, Faculty of Sciences, Aristotle University of Thessaloniki, Thessaloniki, Greece*
[e] *School of Chemical Engineering, Faculty of Engineering, Aristotle University of Thessaloniki, Thessaloniki, Greece*
[f] *Chemical Process & Energy Resources Institute, Centre for Research & Technology Hellas, Thessaloniki, Greece*

ARTICLE INFO

Keywords:
Triangular-like CeO_2 particles
Ni/CeO_2 catalysts
CO_2 methanation
CO oxidation

ABSTRACT

Ceria is a reducible oxide that has been extensively employed as supporting carrier in catalysis due to its unique redox and structural properties in combination with its strong interaction with the active phases. Recently, the synthesis of ceria nanostructures with uniform size and morphology has become a topic of extensive scientific interest in catalysis. Therefore, the combination of earth-abundant and cost-effective transition metals with fine-tuned ceria carriers could provide a platform for multifunctional materials in several energy and environmental applications. Herein, we originally explore the facile synthesis of ceria particles of triangular-like morphology with improved textural and structural characteristics and their subsequent application as supporting carrier of nickel active phase. The as-prepared Ni/CeO_2 catalysts were thoroughly characterized and catalytically assessed for both oxidation (CO oxidation) and reduction (CO_2 hydrogenation) processes to demonstrate the effectiveness of ceria triangular structures as supporting materials in catalysis. The results clearly revealed the pivotal role of ceria nanostructure on the physicochemical properties and in turn on the catalytic performance of the nickel-ceria binary system. The improved reducibility and oxygen kinetics of ceria carrier, along with its abundance in structural defects and Ce^{3+} species, could be considered as the dominant factors towards determining the catalytic performance, offering highly active and selective ceria-based transition metal catalysts.

1. Introduction

Ceria (CeO_2) nanoparticles emerge as prominent catalytic supports or catalysts by themselves in various processes, by exploiting their exceptional characteristics, including oxygen storage capacity, oxygen mobility, strong metal-support interactions, and the rapid interchange between Ce^{3+} and Ce^{4+} oxidation states [1,2]. These distinctive features contribute significantly to the increased catalytic performance observed in ceria-based nanomaterials within the field of heterogeneous catalytic reactions. In recent years, the research interest has focused on thin-layered nanomaterials due to their size-derived unique properties, such as high oxygen exchange kinetics, mechanical strength, and substantial spin diffusion length [3,4]. Advances in the synthesis of CeO_2 nanomaterials are remarkable, exhibiting various nano-morphologies such as nanorods [5,6], nanowires [7], nanotubes [8], nanocubes [8], nanoplates [8] and other structures [9,10], achieved through both chemical and physical methods. However, the synthesis of two-dimensional (2D) CeO_2 structures remains a relatively unexplored topic. In contrast to the well-established synthesis of spherical particles and one-dimensional nanorods/nanowires, the dominance of crystal growth in two dimensions proves challenging, particularly in solution-phase methods. This can be attributed to the inherent complexities of CeO_2, with its cubic crystal structure, and their difficulty for 2D anisotropic growth. Consequently, the synthesis of 2D CeO_2 has been

---

* Corresponding author.
E-mail addresses: sstefa@tuc.gr (S. Stefa), mlykaki@tuc.gr (M. Lykaki), gvarvoutis@uowm.gr (G. Varvoutis), mzografaki@iesl.forth.gr (M. Zografaki), vbinas@chem.auth.gr, binasbill@iesl.forth.gr (V.D. Binas), gmarnellos@cheng.auth.gr (G.E. Marnellos), mkonsolakis@tuc.gr (M. Konsolakis).

https://doi.org/10.1016/j.scenv.2025.100243
Received 10 December 2024; Received in revised form 4 March 2025; Accepted 13 March 2025

reported in a few previous publications [11–15]. Therefore, the synthesis of 2D CeO_2 structures with uniform size and morphology and further elucidation of their formation mechanism are currently topics of intense interest.

Ceria-based transition metal catalysts have shown exceptional catalytic performance due to the synergistic metal-support interactions induced through the fine-tuning of the metal-support interface [1, 16–19]. Ni-based catalysts distinguish themselves with unique advantages. This is attributed to the presence of mobile d-orbital valence electrons in Ni atoms, which for the CO_2 hydrogenation reaction could lead to notable CO_2 conversions at low temperatures, accompanied by exceptional selectivity towards methane production [20–23]. Despite numerous studies into Ni/CeO_2 composites that emphasize on the morphology of the CeO_2 support [5,21,24–31], there is a notable absence of reports on catalysts involving nickel supported on thin-layered CeO_2 nanoparticles.

On the basis of the catalytic processes, CO_2 methanation, also known as the "Sabatier" reaction [25,32], offers a promising approach to utilize captured CO_2 emissions by their combination with green electrolytic hydrogen towards synthetic natural gas production. This exothermic process efficiently converts carbon dioxide (CO_2) into methane (CH_4) by utilizing hydrogen (H_2) as a reactant under relatively mild conditions [23,33]. This approach not only addresses the critical issue of mitigating CO_2 emissions but also provides a clean and storable energy carrier, like methane. By incorporating the power-to-gas (PtG) concept, excess renewable energy can be harnessed to produce methane, facilitating the large scale deployment of renewables through methane storage and distribution in the existing natural gas pipeline networks [34]. Consequently, methane can serve as a versatile clean fuel for a wide range of applications, from heating and power generation to transportation [35]. Moreover, it can be used as a recyclable chemical feedstock in industrial processes [35]. Beyond its energy applications, CO_2 methanation is invaluable in managing CO_2 levels within closed systems, including submarines, spacecrafts, and space stations [36].

The selection of an appropriate catalyst is a crucial prerequisite for overcoming the inherent kinetic barriers in a chemical reaction. Considerable research efforts have been dedicated to exploring a plethora of catalysts for the Sabatier reaction, with numerous catalytic systems extensively reviewed in various works [37–40].

In a similar manner, the abatement of CO through its oxidation over cost-effective catalysts of high activity is of great industrial and environmental interest. The increasing cost of noble metals has steered the scientific community into the development of low cost, highly active and stable catalysts through the fine-tuning of metal oxides via various synthetic and promotional routes [41,42]. Furthermore, CO oxidation can be employed as a probe reaction in order to gain insight into the structure-performance relationships, as shown in previous studies [6, 43].

In this work, we prepared and thoroughly evaluated catalyst composites consisting of nickel supported on CeO_2 triangles (CeO_2 TR) for both reduction and oxidation reactions, namely CO_2 methanation and CO oxidation. These particular processes are selected as probe reactions to explore the effectiveness of the employed synthesis approach on the performance of heterogeneous catalytic systems. Notably, the Ni/CeO_2 TR catalyst exhibited 75 % conversion of CO_2 at 380 °C during its hydrogenation to methane, while in CO oxidation exhibited full conversion at ca. 280 °C. To highlight the superiority of Ni/CeO_2 TR, a comparison with amorphous CeO_2 and Ni/CeO_2 samples was carried out. The results further confirm the improved performance of Ni/CeO_2 TR, showcasing its potential as a catalyst for both reduction and oxidation reactions.

2. Materials and methods

2.1. Materials synthesis

Cerium oxide triangles (CeO_2 TR) were synthesized by the solvothermal method, as thoroughly described in our previous work [44]. In a typical procedure, 3.17 g of cerium acetate and 3 g of urea were dissolved in 30 mL of ethylene glycol (EG) under vigorous stirring for 1 h. Then, the solution was transferred into a Teflon-lined stainless-steel autoclave and heated at 220 °C for 24 h. Afterwards, the autoclave was cooled to room temperature and the solution was centrifuged for 15—20 min. The precipitate was collected and washed twice with ethanol at 6000 rpm for 15 min each. The resulting precipitate was dried at room temperature and calcined at 400 °C for 2 h under air flow (heating ramp of 5 °C/min) in order to obtain the final product. The Ni incorporation into CeO_2 TR sample was accomplished through the wet impregnation method using an aqueous solution of Ni $(NO_3)_2·6H_2O$ so as to obtain a Ni/Ce atomic ratio of 0.25, corresponding to a Ni loading of 8 wt% [30,45,46]. Relevant literature studies over ceria-based mixed oxides have revealed that the optimum redox/surface properties can be obtained in a similar metal content [47–51]. The resulting suspensions were heated under stirring until water evaporation, dried at 90 °C for 12 h, and finally calcined at 500 °C for 2 h (heating ramp of 5 °C/min). For comparison purposes, a commercial ceria sample, CeO_2-comm (Aldrich, 99.9 %, <5 microns), was employed as a carrier for a Ni catalyst of 8 wt% Ni loading (Ni/CeO_2-comm), following the aforementioned synthesis procedure. The actual Ni loading was determined by inductively coupled plasma atomic emission spectroscopy (ICP-AES) and found to be 8.0 ± 0.1 wt%, in agreement with the nominal composition.

2.2. Materials characterization

N_2 adsorption-desorption experiments were performed at –196 °C using a Physisorption Analyzer (NOVA 800, Anton Paar). Prior to the measurements, the samples were degassed at 150 °C for 1 h and 250 °C for 5 h under vacuum. Total surface area was determined via multipoint BET method and the total pore volume was determined at $p/po \approx 0.99$. The mesopores size distribution was determined via the Barrett-Joyner-Halenda (BJH), using the desorption branch data. Structural characterization was performed by X-ray diffraction (XRD) in a Rigaku diffractometer (model RINT 2000, Tokyo, Japan). Morphological characteristics were investigated via Field Emission Scanning Electron Microscopy (FE-SEM, JEOL 7000, JEOL Ltd., Akishima, Tokyo, Japan) operating at 15 keV, equipped with an energy dispersive X-ray spectrometry (EDS) system and Transmission Electron Microscopy (TEM) on a JEM-2100 instrument (JEOL, Tokyo, Japan). Raman measurements were performed at room temperature using a Nicolet Almega XR Raman spectrometer with a 473 nm blue laser as an excitation source. The laser power was 15 mW and the beam was focused on the sample through a confocal microscope equipped with a 50x. X-ray photoelectron (XPS) analysis was conducted on the as-prepared samples using a SPECS FlexMod XPS with 1D-DLD upgraded Detector, and XR-50 Dual Anode X-ray source. All XPS spectra were corrected using the C1s peak at a binding energy of 284.6 eV. Temperature-programmed reduction (H_2-TPR) experiments were carried out in an Automated Chemisorption Flow Analyzer (ChemBET Pulsar TPR/TPD) under H_2 atmosphere, to acquire information on the reducibility of the samples. In a typical TPR experiment, 60 or 80 mg of sample (60 mg for the mixed oxides Ni/CeO_2 και 80 mg for the ceria supports) was placed in a U-shaped quartz cell, located inside an electrical furnace, and heated up to 1100 °C at 10 °C/min under 5 % H_2 in N_2 flow.

2.3. Catalytic evaluation studies

2.3.1. CO_2 methanation

The catalytic studies for the CO_2 methanation reaction were carried out in a quartz fixed-bed U-shaped reactor (i.d. = 1 cm), loaded with 200 mg of catalyst diluted with 200 mg of inert SiO_2. The sample's pretreatment protocol included in situ reduction at 400 °C for 1 h under pure H_2 flow (40 cm^3 min^{-1}), followed by flushing with He (10 cm^3

min^{-1}) until room temperature. The experiments were conducted at 1 bar and in the temperature range of 200 – 500 °C at intervals of 15–20 °C and a heating rate of 1 °C/min. The total volumetric feed flow was 100 cm^3 min^{-1}, corresponding to a weight hourly space velocity (WHSV) of 30 L g^{-1} h^{-1}. The gas feed constituted a pure H_2/CO_2 stoichiometric mixture at a molar ratio of 80/20. Calculations for the thermodynamic equilibrium were derived using the mathematical model RGibbs in Aspen Plus software. The analysis of the reactor outlet mixture was performed in a gas chromatograph with He as the carrier gas, equipped with a thermal conductivity detector (TCD) for the detection of CO and CO_2, separation columns (Molecular Sieve 13X and Porapack QS).

The reactor effluent was passed through a cold trap submerged in an ice bath in order to condense the H_2O produced by the reactions. The only carbonaceous products detected in the reactor outlet stream were CH_4 and CO. The conversion of carbon dioxide (X_{CO2}, %) and product selectivities (S_{CO} and S_{CH4}, %) were calculated as follows (Eqs. (1)–(3)):

$$X_{CO_2} = \frac{([CO_2]_{in} \bullet F_{in}) - ([CO_2]_{out} \bullet F_{out})}{[CO_2]_{in} \bullet F_{in}} \bullet 100 \tag{1}$$

$$S_{CO} = \frac{[CO]_{out}}{[CO]_{out} + [CH_4]_{out}} \bullet 100 \tag{2}$$

$$S_{CH_4} = \frac{[CH_4]_{out}}{[CO]_{out} + [CH_4]_{out}} \bullet 100 \tag{3}$$

The macroscopic reaction rate was defined in terms of the rate of moles of CO_2 consumed per mass of the catalyst, r_m:

$$r_m\left(molCO_2 \bullet g^{-1} \bullet s^{-1}\right) = \frac{[CO_2]_{in} \bullet F_{in} \bullet X_{CO_2}}{100 \bullet 60 \bullet m_{cat} \bullet V_m} \tag{4}$$

where m_{cat} is the mass of the catalyst in grams and V_m is the gas molar volume at 25 °C and 1 bar (24,436 cm^3/mol).

2.3.2. *CO oxidation*

Catalytic tests for CO oxidation were carried out in a quartz fixed-bed reactor (8 mm i.d.), loaded with 100 mg of catalyst (bed volume of 0.25 cm^3). The total flow rate of the feed gas (2000 ppm CO and 1.0 vol % O_2 in He) was 250 cm^3/min, corresponding to a Gas Hour Space Velocity (GHSV) of 60,000 h^{-1}. Catalytic evaluation measurements were carried out by increasing the temperature by 20 degrees steps up to 500 °C. The reactant CO was analyzed by using a CO analyzer (ABB AO2000). The conversion of CO (X_{CO}, %) was calculated by the following equation:

$$X_{CO}(\%) = \frac{[CO]_{in} - [CO]_{out}}{[CO]_{in}} \bullet 100 \tag{5}$$

where $[CO]_{in}$ and $[CO]_{out}$ are the CO concentration (ppm) in the inlet and outlet gas streams, respectively.

The reaction rate was defined in terms of the rate of moles of CO consumed per both mass (r_m), surface area (r_s) and exposed Ni surface area, ($r_{s,Ni}$) of the catalyst (Eqs. (6)–(8)) [46]:

$$r_m\left(mol\ CO \bullet g^{-1} \bullet s^{-1}\right) = \frac{[CO]_{in} \bullet F_{in} \bullet X_{CO}}{100 \bullet 60 \bullet m_{cat} \bullet V_m} \tag{6}$$

$$r_s\left(mol\ CO \bullet m^{-2} \bullet s^{-1}\right) = \frac{r_m}{S_{BET}} \tag{7}$$

$$r_{s,Ni}\left(mol\ CO \bullet m_{Ni}^{-2} \bullet s^{-1}\right) = \frac{r_m}{A_{Ni}} = \frac{r_m \bullet AM_{Ni}}{a_{Ni} \bullet D_{Ni} \bullet N_A} \tag{8}$$

where m_{cat} is the mass of the catalyst in grams, S_{BET} is the surface area of the catalyst in m^2/g, V_m is the gas molar volume at 25 °C and 1 bar (24,436 cm^3/mol), A_{Ni} (m^2/g) is the exposed surface area of Ni per gram of catalyst, AM_{Ni} = 58.69 g/mol is the atomic mass of Ni, $a_{Ni} = 6.51 \bullet 10^{-20}$ m^2 is the atomic cross-sectional area of Ni, D_{Ni} is the nickel dispersion calculated by TEM and $N_A = 6.023 \bullet 10^{23}$ molecules/mol is the Avogadro number.

Moreover, the site time yield (STY) based on the surface Ni content of the samples was calculated (Eq. (9)) in order to assess the intrinsic catalytic activity of the materials [46].

$$STY\left(s^{-1}\right) = \frac{r_m \bullet AM_{Ni}}{w_{Ni} \bullet D_{Ni}} \tag{9}$$

where w_{Ni} is the Ni mass fraction in the sample.

3. Results

3.1. *Materials characterization*

The main textural characteristics of the bare CeO_2 TR and Ni/CeO_2 TR are presented in Table 1. Bare CeO_2 TR demonstrates a very high BET surface area of 115.4 m^2/g while Ni incorporation into the ceria support results in a decrease of the BET surface area (85.0 m^2/g). The pore diameter of CeO_2 TR and Ni/CeO_2 TR is 2.3 and 3.4 nm, respectively. For the commercial samples CeO_2-comm and Ni/CeO_2-comm, the BET surface areas are very low while presenting higher values of average pore diameters, namely 16.8 and 27.5 nm, respectively.

Fig. 1a shows the adsorption-desorption isotherms of bare CeO_2 TR and Ni/CeO_2 TR samples which demonstrate type IV isotherms of IUPAC classification with a hysteresis loop at a relative pressure > 0.5, indicating their mesoporosity. For comparison purposes, the adsorption-desorption isotherms of the commercial samples are also depicted (Fig. 1b). In Fig. 1c and d, the Barrett-Joyner-Halenda (BJH) desorption pore size distributions (PSD) of the samples are shown, with their maxima located at pore diameters higher than 3 nm, corroborating the presence of mesopores. It is noteworthy that the CeO_2 TR and Ni/CeO_2 TR samples show no significant modifications on the basis of pore volume and average pore diameter (Table 1). However, taking into consideration the pore size distribution of the samples (Fig. 1c), the Ni/CeO_2 TR catalyst has a greater amount of larger-sized pores than the bare CeO_2 TR sample, thus exhibiting a lower surface area [44].

The crystal structure analysis of the bare CeO_2 TR and Ni/CeO_2 TR samples, as well as the commercial samples was carried out using X-ray diffraction (XRD), and the corresponding XRD patterns are shown in Fig. 2 and b, respectively. For the bare CeO_2 TR and CeO_2-comm samples, the XRD patterns revealed distinct peaks at $2\theta = 28.5°$, 33.1°, 47.5°, and 56.3°, which can be attributed to the (111), (200), (220), and (311) crystal planes, respectively [6]. These peaks are indicative of the face-centered cubic fluorite structure of ceria (Fm3m symmetry, no. 225, Reference code: 00-043-1002). Upon the addition of nickel to the CeO_2 TR and CeO_2-comm samples, the XRD patterns for the Ni/CeO_2 TR and Ni/CeO_2-comm samples exhibited additional diffraction peaks. Specifically, at $2\theta = 37.3°$ and 43.4°, the observed peaks can be associated with the (111) and (200) crystal planes, respectively [35,52]. These peaks can be attributed to the typical cubic structure of NiO (Reference code: 01-075-0197). Therefore, the XRD analysis confirms that the Ni/CeO_2 TR sample exhibits a combination of the face-centered cubic fluorite structure of ceria and the cubic structure of NiO.

In addition to the XRD analysis, the average crystallite size (D_{XRD}) of the as-obtained samples was determined using the Scherrer equation. The results are summarized in Table 2. The bare CeO_2 TR sample exhibited an average crystallite size of 9.1 nm. Upon the addition of NiO

Table 1
Textural characteristics of bare CeO_2 TR and Ni/CeO_2 TR.

Sample	S_{BET} (m^2/g)	V_{pore} (cm^3/g)	d_{pore} (nm)
CeO_2 TR	115.4	0.066	2.3
Ni/CeO_2 TR	85.0	0.072	3.4
CeO_2-comm	1.48	0.0062	16.8
Ni/CeO_2-comm	3.23	0.022	27.5

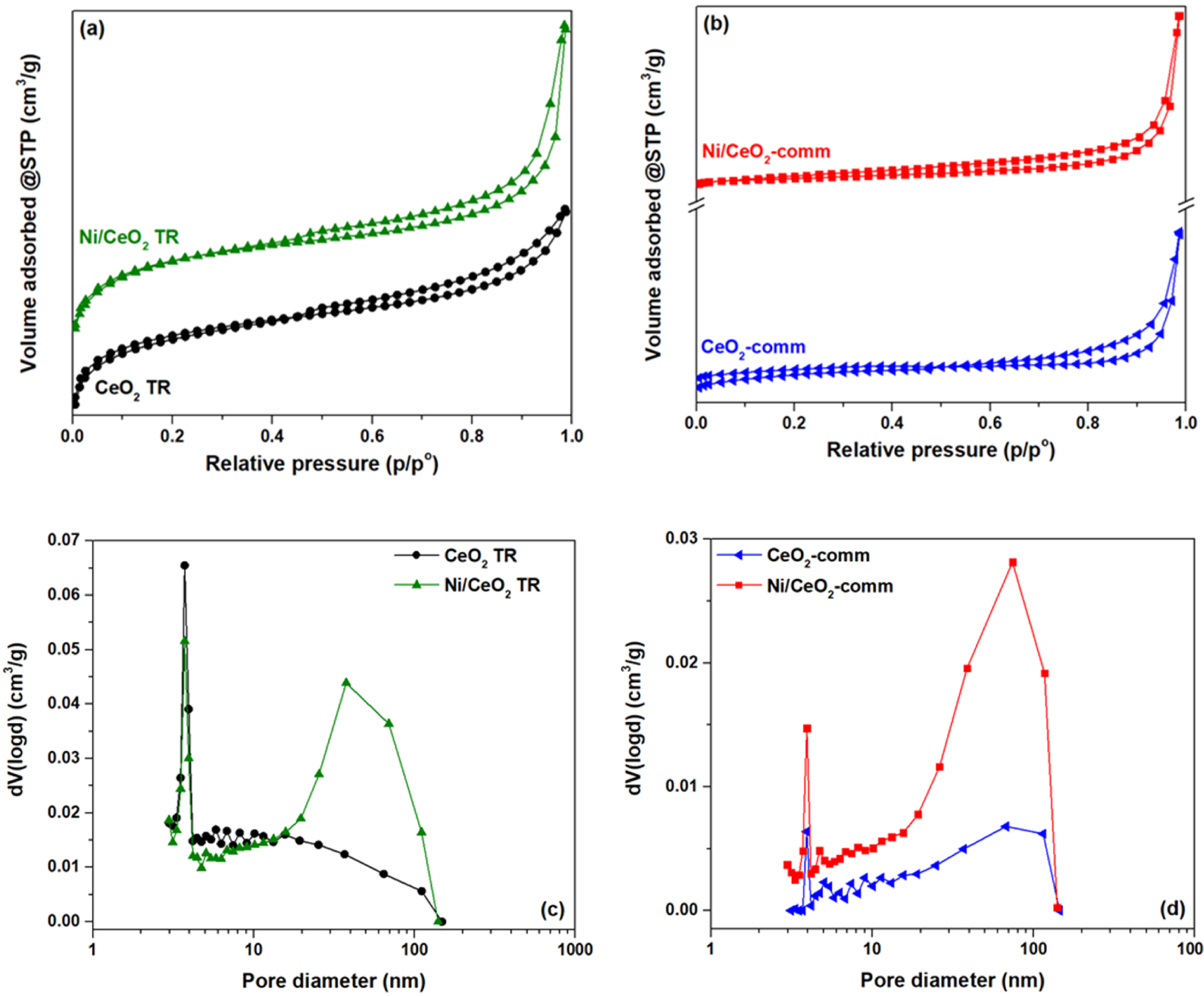

Fig. 1. Adsorption-desorption isotherms of (a) CeO_2 TR, Ni/CeO_2 TR and (b) CeO_2-comm, Ni/CeO_2-comm samples; BJH desorption pore size distributions (PSD) of (c) CeO_2 TR, Ni/CeO_2 TR and (d) CeO_2-comm, Ni/CeO_2-comm samples.

into the CeO_2 TR sample (Ni/CeO_2 TR), a small increase in the ceria crystallite size was observed, with a value of 9.9 nm, while the crystallite size of NiO was estimated to be ca. 28.0 nm. These values, in conjunction with the morphological characteristics of ceria particles (Figs. 3 and 4), indicate that the ceria triangular particles are polycrystalline in nature, consisting of nanoscale crystallites that form larger aggregates. On the other hand, the crystallite size of NiO is much higher compared to that of ceria, despite its lower content (8 wt%), implying an aggregation of NiO phase over ceria particles. Similar results have been previously obtained for several ceria-based catalysts (e.g. Cu, Co, Fe) of similar metal loading [6,43,53].

Furthermore, the d-spacing, lattice parameter, and unit cell volume were calculated based on the most intense planar reflection of CeO_2 (111) for the Ni/CeO_2 TR sample. It was found that these parameters were lower in the Ni/CeO_2 TR sample compared to the bare CeO_2 TR sample. This change in lattice parameters is also evident in the shift of the diffraction angle, as depicted in Fig. 2b. The contraction of the ceria lattice in the Ni/CeO_2 TR sample can be attributed to the incorporation of nickel oxide, which has smaller ionic radii compared to cerium ions [54–56]. The presence of these smaller ions in the ceria lattice causes a reduction in the interatomic distances and leads to a contraction of the lattice. This phenomenon is consistent with the observed changes in lattice parameters and the shift in the diffraction peaks. In this point, it should be mentioned that the commercial samples exhibit much larger values of the average ceria crystallite sizes, namely 57.5 and 60.1 nm for the CeO_2-comm and Ni/CeO_2-comm samples, respectively (Table 2). These findings in conjunction to the previously shown BET analysis, clearly reflect the pronounced structural and textural properties of CeO_2 particles of triangular-like morphology as compared to commercial ones.

The morphology of bare CeO_2 TR and Ni/CeO_2 TR was determined by SEM and TEM analyses. More specifically, from SEM analysis, the CeO_2 TR sample exhibits a triangle-like morphology, which is retained upon the addition of nickel, as illustrated in Fig. 3a and b. In contrast, the CeO_2-comm sample displays an irregular morphology (Fig. 3c), while Ni/CeO_2-comm consists of an irregular agglomeration of CeO_2 and nano-sized NiO particles (Fig. 3d).

To further investigate the elemental distribution, field-emission scanning electron microscopy (FE-SEM) equipped with energy-dispersive X-ray spectroscopy (EDS) was performed on the Ni/CeO_2 TR and Ni/CeO_2-comm samples (Fig. 3e and f). The FE-SEM/EDS analysis confirms the uniform distribution of Ce and Ni in both samples. Additionally, EDS quantification of Ni/CeO_2 TR determined an atomic Ni/Ce ratio of 0.26 and a Ni loading of 8.1 wt%, values that closely

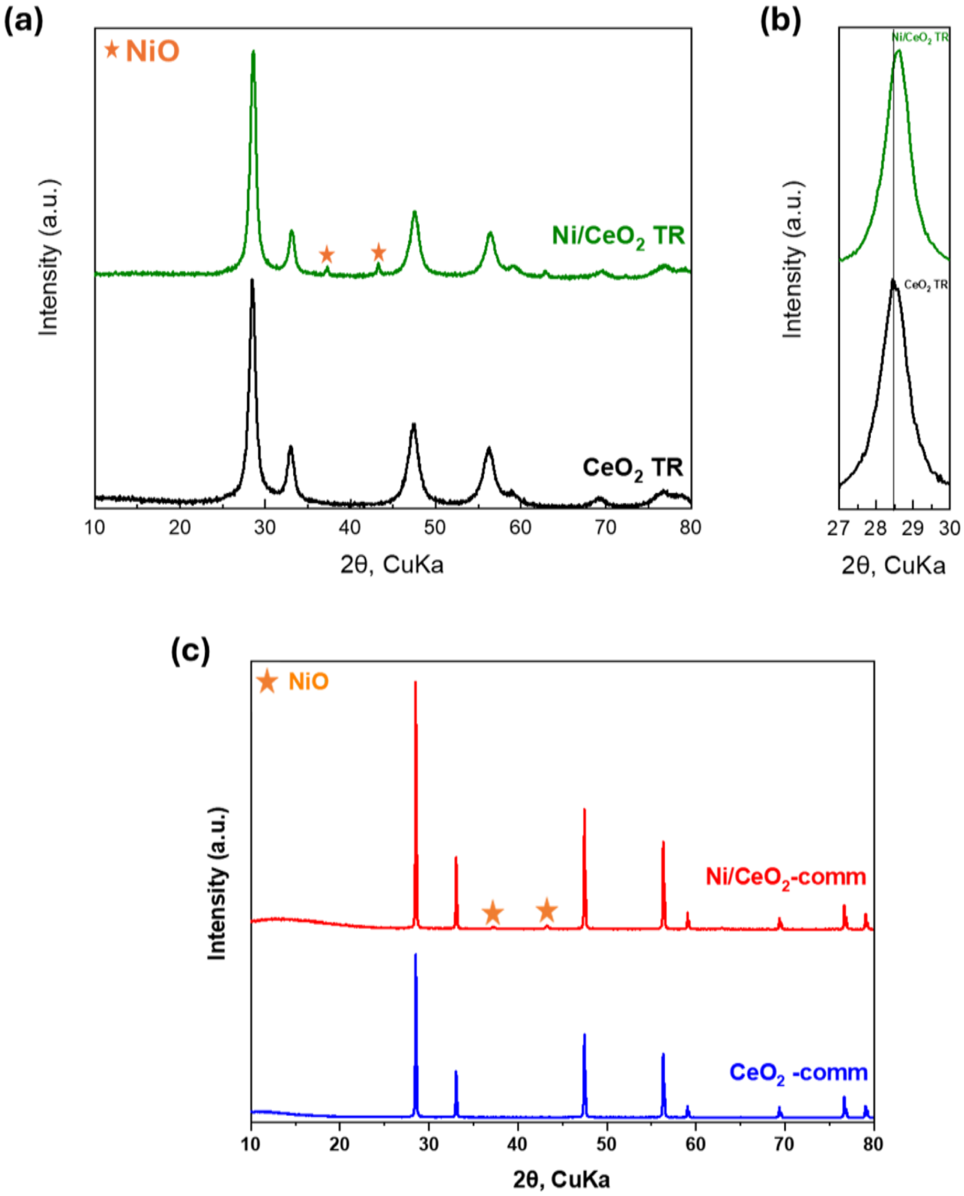

Fig. 2. XRD patterns of (a) CeO_2 TR, Ni/CeO_2 TR, (b) the (111) diffraction peak of CeO_2 and (c) CeO_2-comm, Ni/CeO_2-comm samples.

Table 2
Structural and morphological characteristics of bare CeO_2 TR, Ni/CeO_2 TR, CeO_2-comm and Ni/CeO_2-comm.

Sample	XRD Analysis					TEM Analysis		Raman Analysis
	CeO_2 (111)			D_{XRD} (nm)		Ni particle size (nm)	D_{Ni} (%)	I_D/I_{F2g}
	$d_{(111)}$ spacing (nm)	Lattice Parameter (nm) a = b = c	Unit Cell Volume $(nm)^3$	CeO_2 (111)	NiO (200)			
CeO_2 TR	0.313	0.5422	0.1594	9.1	—	—	—	0.024
Ni/CeO_2 TR	0.312	0.5406	0.1580	9.9	28.0	28.1 ± 6.0	3.6	0.63
CeO_2-comm	0.313	0.5416	0.1589	57.5	—	—	—	—
Ni/CeO_2-comm	0.313	0.5416	0.1589	60.1	26.3	24.2 ± 3.9	4.2	—

match the nominal composition (Ni/Ce = 0.25, 8 wt% Ni) and are consistent with the surface elemental composition obtained by XPS analysis (see below). Similarly, the Ni/Ce atomic ratio and Ni loading for Ni/CeO_2-comm were calculated as 0.25 and 7.8 wt%, respectively.

Additionally, the TEM images of CeO_2 TR, Ni/CeO_2 TR, CeO_2-comm, and Ni/CeO_2-comm are depicted in Fig. 4. The triangle-like morphology of the CeO_2 TR is also confirmed through TEM analysis (Fig. 4a), while it remains unchanged with the incorporation of NiO (Fig. 4b). Moreover, separated NiO particles of sphere-like morphology are detected, as shown in Fig. 4b and c. The high-resolution TEM (HRTEM) analysis of Ni/CeO_2 TR (Fig. 4f) reveals a lattice spacing of 0.21 nm, corresponding to the NiO (200) planes in contact with CeO_2 TR, in agreement with the XRD results (Fig. 2). The mean particle size of NiO was estimated by TEM analysis and the results are presented in Fig. 4b and Table 2. From

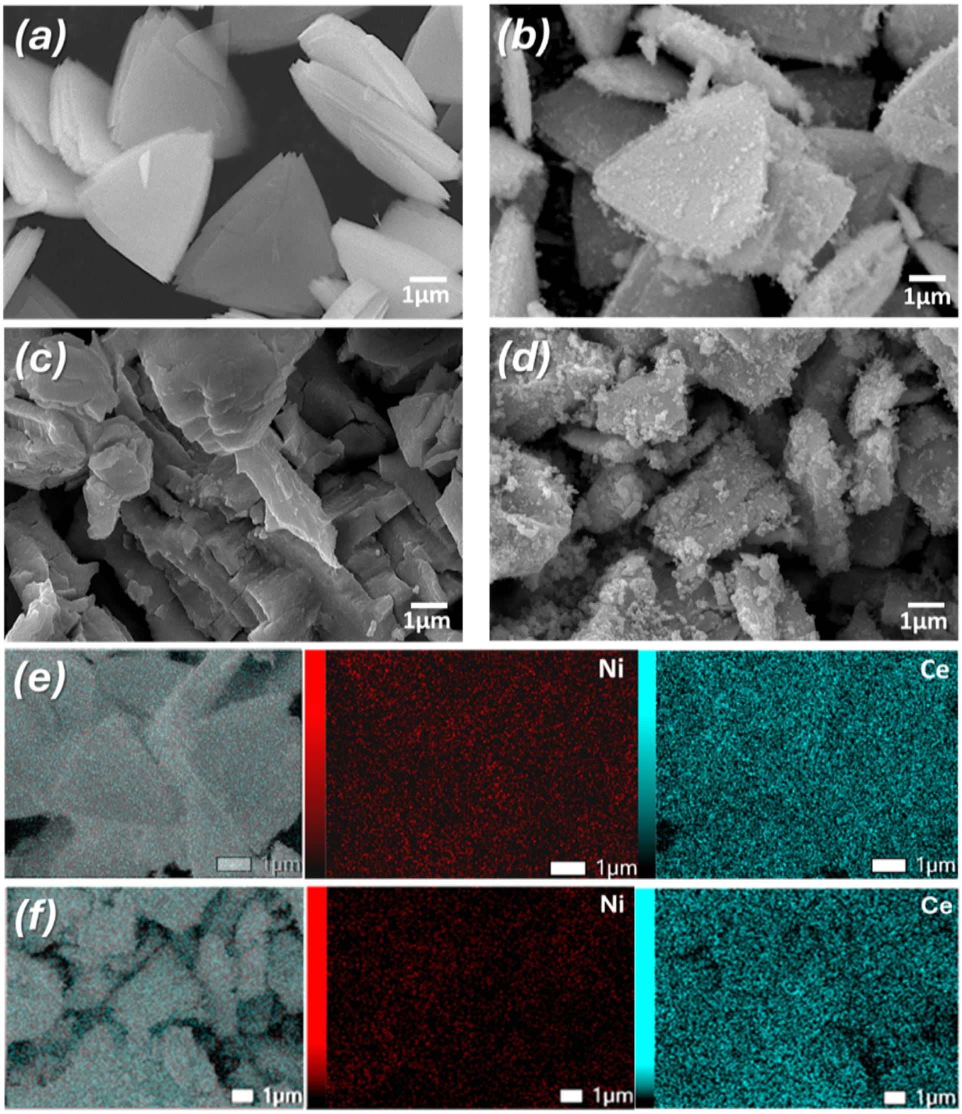

Fig. 3. SEM images of the samples: (a) CeO_2-TR, (b) Ni/CeO_2 TR, (c) CeO_2-comm, (d) Ni/CeO_2-comm; SEM-EDS elemental mapping images: (e) Ni/CeO_2 TR, (f) Ni/CeO_2-comm.

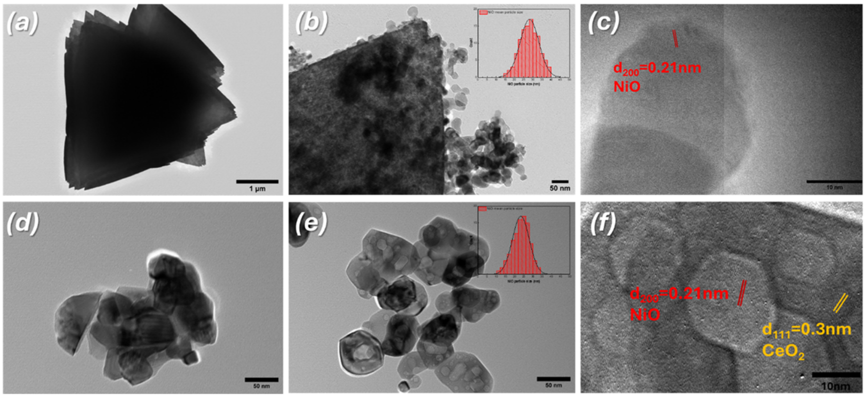

Fig. 4. TEM images of the samples: (a) CeO_2 TR, (b) Ni/CeO_2 TR, (d) CeO_2-comm, (e) Ni/CeO_2-comm; HRTEM images: (c) Ni/CeO_2 TR, (f) Ni/CeO_2-comm.

the particle size distribution (PSD) analysis, the NiO particle size was estimated at 28.1 nm, which is in full agreement with the XRD analysis (Table 2).

Furthermore, TEM analysis was performed for CeO_2-comm and Ni/CeO_2-comm, as shown in Fig. 4d and e. The CeO_2-comm sample exhibits an irregular morphology with relatively large particles (Fig. 4d). Following NiO incorporation, the Ni/CeO_2-comm sample appears as a mixture of large CeO_2 particles and smaller NiO particles (Fig. 4e). The

HRTEM image of Ni/CeO_2-comm (Fig. 4f) confirms the presence of NiO and CeO_2 phases, with lattice spacings of 0.21 nm and 0.3 nm, respectively. This indicates that NiO (200) planes are in contact with CeO_2 (111) planes, further corroborating the XRD results. From the PSD analysis of Ni/CeO_2-comm, the average NiO particle size was found to be 24.2 nm, which is in good agreement with the XRD results (Table 2). Based on the TEM particle sizes, Ni dispersion was found to be 3.6 % for Ni/CeO_2 TR and 4.2 % for the commercial Ni/CeO_2 sample (Table 2).

Fig. 5 depicts the Raman spectra of bare CeO_2 TR and Ni/CeO_2 TR samples. For bare CeO_2 TR support, the characteristic F_{2g} mode at 457 cm^{-1} is observed which is attributed to the Fm3m fluorite cubic ceria structure, and a weak band at ~250 cm^{-1} which is ascribed to second-order transverse acoustic mode [57]. Moreover, a wide band in the 530 and 700 cm^{-1} region, which is commonly called the defect-induced band (denoted as the "D" band), can be attributed to structural perturbations of the ceria cubic lattice [57–59]. With the addition of NiO into ceria, a small red shift of the F_{2g} peak is observed, as well as a decrease in intensity. In addition, in the case of Ni/CeO_2 TR, the wide D band significantly exhibits increased intensity, which is related to punctual defects and oxygen vacancies due to the incorporation of NiO. Therefore, the I_D/I_{F2g} ratio is associated with the abundance of structural defects [60]. The I_D/I_{F2g} values for both CeO_2 TR and Ni/CeO_2 TR were calculated and presented in Table 2. Particularly, the I_D/I_{F2g} ratio for bare CeO_2 TR is very low (0.024) while a significant increase in this ratio is observed for Ni/CeO_2 TR (0.63), revealing the remarkable impact of nickel-ceria synergistic interactions towards the increased population of structural defects and oxygen vacancies of Ni/CeO_2 TR.

The XPS analysis was performed to determine the oxidation states and surface composition in the CeO_2 TR and Ni/CeO_2 TR samples. The deconvolution of the Ce 3d and Ni 2p spectra was conducted using a combination of Gaussian-Lorentzian peak fitting after applying a Shirley background correction. Fig. 6a shows the Ce 3d XPS spectra of bare CeO_2 TR and Ni/CeO_2 TR samples. The Ce3d curves were deconvoluted into eight peaks. More specifically, the "u" peaks refer to the spin-orbit coupling $3d_{5/2}$ while the "v" peaks correspond to the spin-orbit coupling $3d_{3/2}$ [5,23,61,62]. The v''', v'', v, u''', u'', and u peaks are attributed to Ce^{4+} and the v' and u' are ascribed to Ce^{3+} [5,23,61].

Additionally, Table 3 summarizes the results obtained from XPS analysis for both bare CeO_2 TR and Ni/CeO_2 TR. The ratio of Ce^{3+} ions to the whole peak area in the Ce 3d region is calculated from the area ratio of the sum of the Ce^{3+} species to that of the total cerium species. Bare CeO_2 exhibits an amount of Ce^{3+} species of 25.6 % while Ni/CeO_2 TR shows a much higher population of Ce^{3+} ions (44.8 %). The presence of oxygen vacancies is directly correlated with the increase in Ce^{3+} concentration, as the vacancies facilitate the reduction of Ce^{4+} ions. More specifically, the stoichiometric CeO_2 can be transformed into non-stoichiometric CeO_{2-y} by releasing oxygen and reduction of Ce^{4+} to Ce^{3+} with the simultaneous formation of the oxygen vacancies into the lattice structure [63]. It is worth mentioning that the Ce^{3+} species are associated with the abundance of oxygen vacancies and the extent of metal–support interactions [33,64]. Therefore, these findings indicate the presence of more oxygen vacancies, in the case of Ni/CeO_2 TR compared to that of bare support material which is in full agreement with the Raman analysis. Notably, the larger increase in the Raman D band area (Fig. 5) compared to the increase of XPS-measured Ce^{3+} concentration upon the Ni incorporation into CeO_2 TR suggests a complex defect structure. The Raman technique is more sensitive to the overall defect concentration and distribution, while XPS provides information about the average Ce^{3+} oxidation state on the surface [65,66]. This combined information offers a more comprehensive understanding of the structural and electronic modifications induced by Ni incorporation into CeO_2 TR.

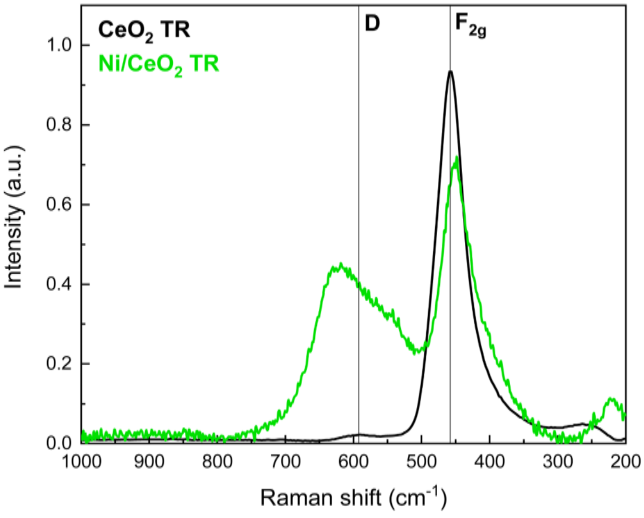

Fig. 5. Raman spectra for bare CeO_2 TR and Ni/CeO_2 TR.

The high-resolution spectrum of Ni $2p_{3/2}$ is presented in Fig. 6b, implying the formation of Ni^{2+} species on the surface of the Ni/CeO_2 TR catalyst. Moreover, the Ni/Ce XPS atomic ratio is found to be 0.23 (Table 3), in perfect agreement with EDS analysis (see above) and the nominal composition of Ni (8 wt% corresponding to a Ni/Ce ratio of 0.25). To further clarify, the nominal atomic ratios, based on the nominal catalyst composition, are Ni/Ce = 0.25, O/Ce = 2 and O/Ni = 8. The XPS analysis reveals slightly lower Ni/Ce (~0.23) and higher O/Ce (~2.43) and O/Ni (~10.54) ratios, which could be attributed to surface enrichment in oxygen species. These findings demonstrate, once again, the pronounced structural characteristics of ceria triangles, which facilitate the formation of oxygen vacancies and in turn Ce^{3+} sites via metal-support interactions.

TPR experiments were also conducted to investigate the redox properties of the as-prepared samples. Fig. 7 presents the reduction profiles of bare CeO_2 TR and Ni/CeO_2 TR, as well as of the commercial samples. Bare CeO_2 TR consists of two broad peaks centered at ca. 500 °C and 860 °C that can be ascribed to ceria surface oxygen (O_s) and bulk oxygen (O_b) reduction, respectively [67]. Also, the O_s peak is accompanied by a shoulder peak at 345 °C which could be related to the peculiar pyramid-like morphology of ceria, as previously evidenced in ceria nanoparticles of distinct morphology [67]. Interestingly, the commercial ceria sample (CeO_2-comm) exhibits only the O_b peak at 890 °C. The addition of nickel has a significant positive impact on its overall reducibility, as evidenced by the larger reduction peaks and the shifts towards lower temperatures as compared to the corresponding bare ceria supports. Specifically, Ni/CeO_2 TR exhibits four distinct reduction peaks at 182, 267, 368, and 850 °C; the first two peaks, starting at 182 °C while reaching a maximum at 267 °C, are ascribed to the reduction of adsorbed oxygen species caused by the formation of Ni–O–Ce structures [60,68], the peak at 368 °C is associated with the well-dispersed NiO phase interacting strongly with ceria (the so-called boundary Ni–O–Ce) whereas the shoulder peak above 480 °C can be attributed to the reduction of the phase-separated surface NiO clusters over the ceria support [60,69,70]. It should also be mentioned that Pantaleo et al. [71] have attributed the low-temperature TPR peaks to the reduction of NiO particles of different sizes. In contrast to the triangular-shaped nickel-ceria catalyst, the commercial sample exhibits only one wide peak at 394 °C. The high-temperature peaks at 850 and 862 °C in the Ni/CeO_2 TR and Ni/CeO_2-comm samples, respectively, are related to ceria bulk oxygen reduction. Comparing the TPR profiles (Fig. 6) between the triangular-shaped samples and the commercial ones, the pivotal role of support morphology in the low-temperature reducibility is evident.

Table 4 presents the hydrogen consumption of bare CeO_2 TR and Ni/CeO_2 TR, as well as of the commercial samples. Bare CeO_2 TR shows a surface-to-bulk oxygen ratio of 0.92 while exhibiting a total H_2 consumption of 1.25 mmol H_2/g. The incorporation of Ni into the ceria

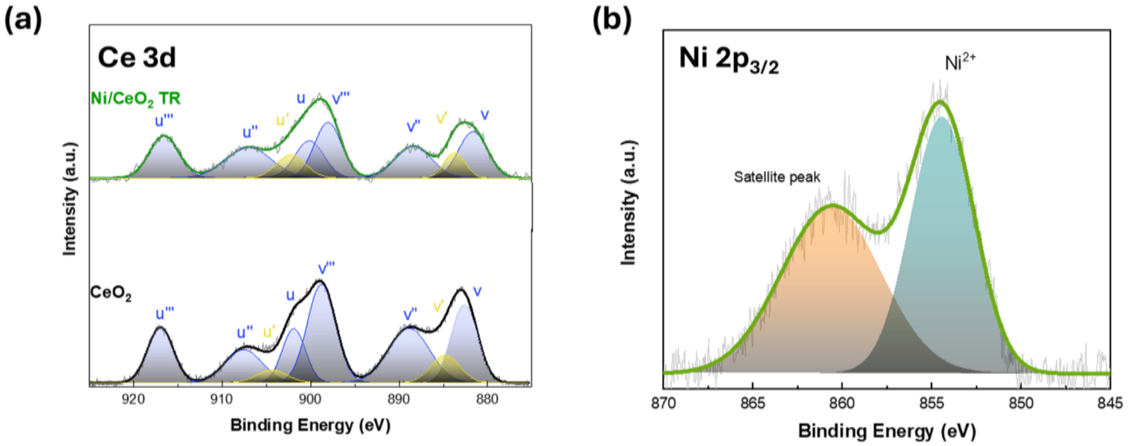

Fig. 6. (a) XPS spectra of Ce 3d for bare CeO_2 TR and Ni/CeO_2 TR; (b) XPS spectrum of Ni $2p_{3/2}$ for Ni/CeO_2 TR.

Table 3
Surface atomic compositions, Ni/Ce ratio and content of Ce^{3+} determined from XPS analysis for bare CeO_2 TR and Ni/CeO_2 TR samples.

Sample	Ce (at%)	Ni (at%)	O (at%)	Ni/Ce	Ce^{3+} (%)
CeO_2 TR	33.8	—	66.2	—	25.6
Ni/CeO_2 TR	27.3	6.3	66.4	0.23	44.8

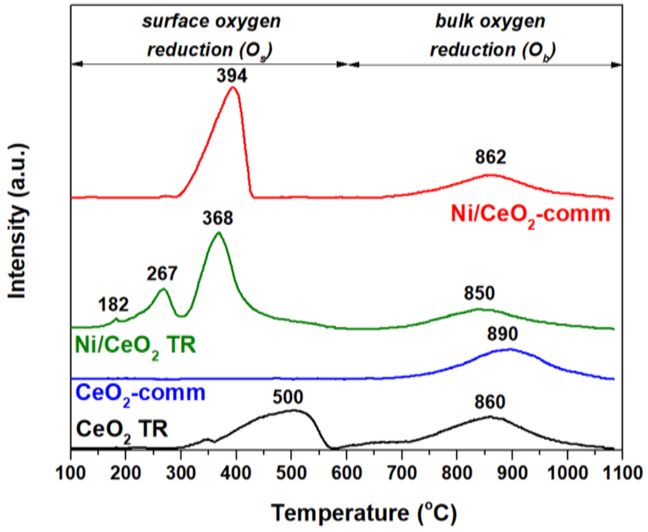

Fig. 7. H_2-TPR profiles of the triangular-shaped and commercial samples.

Table 4
Redox properties of the triangular and commercial samples.

Sample	H_2 consumption (mmol H_2/g_{cat})[a]			O_s/O_b
	O_s	O_b	Total	
CeO_2 TR	0.60	0.65	1.25	0.92
Ni/CeO_2 TR	1.50	0.50	2.00	3.0
CeO_2-comm	—	0.56	0.56	—
Ni/CeO_2-comm	1.08	0.57	1.65	1.89

[a] Estimated by the area of the corresponding TPR peaks at temperatures T < 600 °C (O_s) and T > 600 °C (O_b), calibrated against a known amount of CuO standard sample.

carrier results in a notable increase of H_2 uptake in the low-temperature range, resulting in a surface-to-bulk oxygen ratio of 3.0 (Table 4). The latter implies the abundance of surface oxygen species upon nickel incorporation, which could play a dominant role in catalysis, as further discussed below. Regarding the commercial samples, CeO_2-comm, exhibiting only the bulk oxygen reduction peak, shows a hydrogen consumption of 0.56 mmol H_2/g while the Ni/CeO_2-comm catalyst exhibits much lower values of total H_2 consumption (1.65 mmol H_2/g) and surface-to-bulk oxygen ratio (1.89) than the triangular-shaped catalyst (Table 4), revealing once again the key role of ceria morphology in the redox behavior of the materials.

3.2. *Catalytic evaluation studies*

3.2.1. *CO_2 methanation*

The CO_2 hydrogenation performance of bare CeO_2 TR and Ni/CeO_2 TR catalysts was explored within a temperature range of 200—400 °C. Fig. 8a presents the CO_2 conversion profiles of both catalysts, comparing them to the thermodynamic equilibrium conversion profiles for methanation and reverse water-gas shift (rWGS) reactions. The results clearly demonstrate the superior methanation performance of the Ni/CeO_2 TR catalyst, indicating the advantageous effect of combining Ni metal with the ceria-triangles support. Importantly, the Ni/CeO_2 TR catalyst exhibited an onset methanation temperature of approximately 245 °C, while the bare CeO_2 TR showed negligible reactivity in the whole temperature range. Furthermore, it is noteworthy that the as-synthesized Ni/CeO_2 TR catalyst displayed complete selectivity towards methane at all investigated temperatures, in contrast to bare CeO_2 TR (Fig. 8b).

To further highlight the enhanced catalytic performance of Ni/CeO_2 TR, a comparison was elaborated with the corresponding commercial samples, CeO_2-comm and Ni/CeO_2-comm, as shown in Fig. 8. The comparison clearly demonstrates that Ni/CeO_2 TR is significantly more active and selective towards CH_4 formation as compared to Ni/CeO_2-comm, underscoring the crucial role of the ceria triangular support, while the CeO_2-comm sample shows also negligible activity as is the case for CeO_2 TR. Regarding methane selectivity, at 300 °C, CeO_2-comm and Ni/CeO_2-comm exhibit CH_4 selectivity values of 22 % and 63 %, respectively. In contrast, CeO_2 TR and Ni/CeO_2 TR display methane selectivity values of 3 % and 98.1 %, respectively. These results provide clear evidence that the presence of the nickel active phase is indispensable to activate CO_2 and generate methane. Although bare CeO_2 TR exhibits negligible catalytic performance, when combined with Ni, the catalytic activity is significantly promoted, leading to conversion and methane selectivity values close to 75 % and 100 %, respectively, at 380 °C. In contrast, the corresponding modifications on the commercial Ni/CeO_2-comm sample are noticeably less prominent. Furthermore, short-term (24 h) stability tests (not shown for brevity) were performed over the optimum triangular-shaped catalyst (Ni/CeO_2 TR), revealing its stable performance with no deterioration of activity or selectivity.

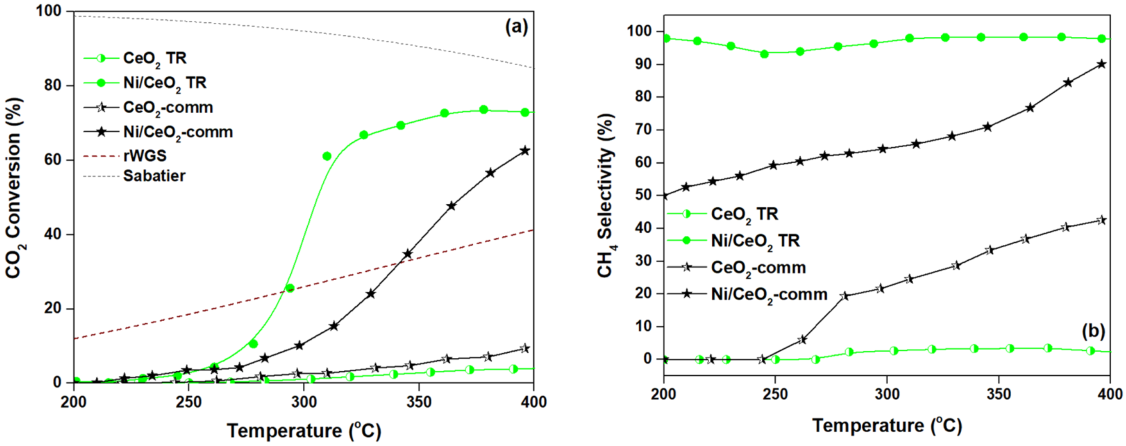

Fig. 8. (a) CO_2 conversion and (b) CH_4 selectivity versus temperature for CeO_2-comm, Ni/CeO_2-comm, CeO_2 TR and Ni/CeO_2 TR catalysts. Reaction conditions: WHSV = 30 $L{\bullet}g^{-1}{\bullet}h^{-1}$, H_2:CO_2 = 4, P = 1 atm.

The superior performance of Ni/CeO_2 TR for the methanation of CO_2 could be attributed to the enhanced redox properties and oxygen mobility of ceria's triangular-like structure. Moreover, Ni/CeO_2 TR exhibits abundance in structural defects and oxygen vacancies, as corroborated by both Raman and XPS analyses (see above). More specifically, nickel facilitates the dissociation of H_2 into hydrogen ad-atoms on the catalyst surface [72], which eventually lead to the formation of methane through the hydrogenation of the species formed by the adsorption of CO_2 [73]. The Ni/CeO_2 TR sample exhibits high CO_2 methanation performance, in terms of both conversion and selectivity, due to the synergistic interactions between nickel and the triangular-like ceria structure, resulting in improved reducibility and abundance in structural defects and oxygen vacancies.

In this point, it should be noted that although the attained catalytic performance is not superior as compared to the state-of-the-art Ni/CeO_2 nanocomposites (e.g. Y_{CH4} = 92 % at T < 300 °C [18,46]), the unique textural, structural and mechanical characteristics of triangular-like CeO_2 structures could render them as promising candidates for large scale production and commercial applications [74,75]. In Table 5, the CO_2 methanation performance in terms of CO_2 conversion (X_{CO_2}) and CH_4 selectivity (S_{CH_4}) over ceria-based Ni catalysts of various morphologies (triangles, nanorods, nanopolyhedra, etc.) and of similar porous and structural characteristics are summarized. It is evident that the combination of nickel with ceria of specific morphology gives rise to extremely active catalytic systems for the methanation of CO_2. It is also worth mentioning that the triangular-shaped ceria can be considered as a promising support for the incorporation of the active metal phase.

In general, CO_2 methanation follows two main reaction paths, namely the CO and the formate routes. In the CO pathway, gaseous CO_2 is directly dissociated to *CO (intermediate carbonyl) and *O species, followed by their hydrogenation to *CH_4 and the subsequent desorption of gas-phase CH_4 [19,77,81,82]. In the latter pathway, the main intermediates are the formate species (*HCOO) instead of the carbonyls. During this route, the formate species react with the chemisorbed hydrogen adatoms [81–83]. Taking into account the hydrogen activation mechanism over metal-ceria catalysts, gas-phase hydrogen is activated via dissociation on the metal particles. Then, the migration of the adsorbed hydrogen adatoms on the CeO_2 support takes place via spillover. Consequently, they react with carbon-containing intermediates towards the formation of gas-phase CH_4 [84].

On the basis of the above mechanistic discussion, Ni/CeO_2 triangles exhibit superior CO_2 methanation performance in comparison to the commercial sample (Ni/CeO_2-comm), arising mainly from the synergistic metal-support interactions which enable hydrogen activation and

Table 5
Summary of Ni-ceria catalysts of different morphology for CO_2 methanation at H_2:CO_2 = 4 and P = 1 bar.

Sample	Ni loading (wt%)	S_{BET} (m^2/g)	D_{XRD} CeO_2 (111)	WHSV (L g^{-1} h^{-1})	T (°C)	X_{CO_2} (%)	S_{CH_4} (%)	Ref.
Ni/CeO_2 TR (triangles)	8	85.0	9.9	30	380	75	100	This work
Ni/CeO_2-comm (amorphous)	8	3.23	60.1	30	380	56	84	This work
Ni/CeO_2-NR (nanorods)	7.9	72	14	30	300	92.1	99.8	[30]
Ni/CeO_2-NR (nanorods)	13.38	32	18.1	300	400	53.1	46.1	[69]
Ni/CeO_2-NR (nanorods)	8.92	89.8	10.3	20	250	90.4	90	[76]
Ni/CeO_2-NP (polyhedra)	10	56	9.5	21	250	41	99	[21]
Ni/CeO_2-NPs (nanoparticles)	5	89.8	10.3	12	350	84.3	100	[77]
Ni/CeO_2-NR (nanorods)	*	34.6	6.7	80.8	320	74.1	99	[78]
Ni/CeO_2-NW (nanowires)	10	62.3	—	60	325	91.5	94.4	[79]
Ni/CeO_2-NB (broom-like)	9.68	112.1	—	36	240	67.5	99.6	[80]

[*] molar ratio Ni:Ce = 3:7.

dissociation, thus resulting in enhanced methane formation.

3.2.2. CO oxidation

Bare CeO_2 TR and Ni/CeO_2 TR catalysts along with the corresponding commercial samples CeO_2-comm and Ni/CeO_2-comm were also catalytically evaluated in the oxidation of CO (Fig. 9). In terms of half-conversion temperature (T_{50}), the following oxidation performance was obtained: Ni/CeO_2 TR (135 °C) > Ni/CeO_2-comm (235 °C) > CeO_2 TR (246 °C) > CeO_2-comm (452 °C). The addition of nickel into the ceria supports considerably enhances the catalytic activity. The triangular-like Ni/CeO_2 TR sample exhibits the best CO oxidation performance, offering 99 % CO conversion at 275 °C. Also, it should be mentioned that the optimum Ni/CeO_2 TR catalyst exhibited a stable conversion performance in short-term (24 h) stability experiments (not shown for brevity).

Table 6 summarizes the CO oxidation performance in terms of half-conversion temperature (T_{50}) over ceria-based Ni catalysts of various morphologies (e.g., triangles, nanorods, nanopolyhedra) and of similar porous and structural characteristics. For comparison purposes the corresponding performance of commercial ceria samples is included in the Table. The superior performance of ceria-based samples of distinct morphology in comparison to the amorphous commercial ceria is obvious, highlighting the pivotal role of support structure and morphology. Among the differently shaped catalysts, Ni-ceria nanorods exhibit the best CO oxidation performance ($T_{50} = 121$ °C) [58] followed by the triangular-shaped catalyst (Ni/CeO_2 TR, $T_{50} = 135$ °C) developed in the present work. It can be therefore deduced that the fine-tuning of ceria shape and its combination with a suitable metal as the active phase can lead to binary catalytic systems of superior oxidation performance, as thoroughly elaborated in our previous studies [16,17].

Table 7 shows the specific activity, normalized per unit of catalyst mass (nmol g^{-1} s^{-1}), surface area (nmol m^{-2} s^{-1}) and exposed Ni surface area (nmol m_{Ni}^{-2} s^{-1}), as well as the site time yield (STY, s^{-1}) at differential conditions ($X_{CO} < 20$ %, T = 100 °C, GHSV = 60,000 h^{-1}), which can reflect more accurately the intrinsic reactivity of the as-prepared catalysts. It is evident that Ni/CeO_2 TR exhibits by far the best catalytic performance, in terms of both conversion and specific activity. Moreover, it presents a site time yield value greater by two orders of magnitude than the equivalent commercial sample, indicating its superior intrinsic reactivity. On the basis of the present findings, the superior catalytic behaviour of the Ni/CeO_2 TR sample can be mainly ascribed to its enhanced reducibility and oxygen kinetics, originated from the strong interaction between ceria triangles and nickel species, along with the abundance of the support in oxygen vacancies, as previously evidenced through Raman and XPS analyses.

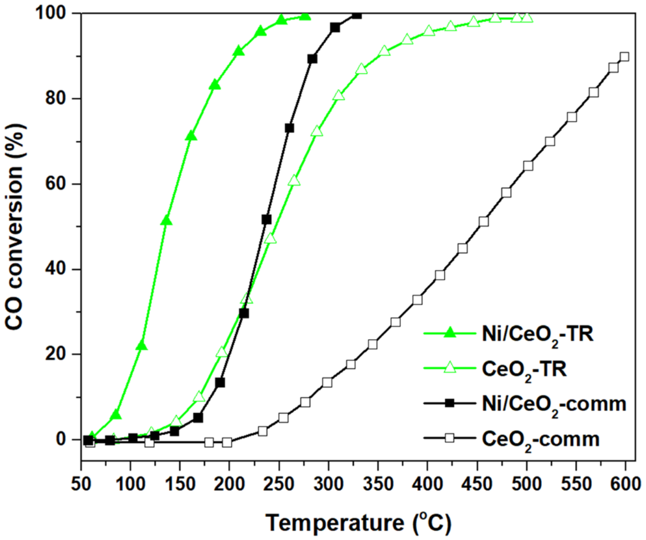

Fig. 9. CO conversion as a function of temperature for CeO_2-comm, Ni/CeO_2-comm, CeO_2 TR, and Ni/CeO_2 TR catalysts. Reaction conditions: 2000 ppm CO, 1 vol% O_2, GHSV = 60,000 h^{-1}.

Table 6
Summary of Ni-ceria catalysts of different morphology for CO oxidation.

Sample	Ni loading (wt%)	S_{BET} (m^2/g)	D_{XRD} CeO_2 (111)	GHSV (h^{-1})	T_{50} (°C)	Ref.
CeO_2 TR (triangles)	—	115.4	9.1	60,000	246	This work
CeO_2-comm (amorphous)	—	1.48	57.5	60,000	452	This work
Ni/CeO_2 TR (triangles)	8	85.0	9.9	60,000	135	This work
Ni/CeO_2-comm (amorphous)	8	3.23	60.1	60,000	235	This work
CeO_2-NR (nanorods)	—	91.8	13.2	39,000	320	[6]
CeO_2-NP (nanopolyhedra)	—	109.4	9.5	39,000	350	[6]
CeO_2-NC (nanocubes)	—	39.5	19.2	39,000	385	[6]
CeO_2-NR (nanorods)	—	66	—	40,000[a]	202	[58]
CeO_2-NR (nanorods)	—	108	8.4	28,800	312	[85]
CeO_2-HS (hollow spheres)	—	36.3	—	18,000[a]	334	[86]
Ni/CeO_2-NR (nanorods)	10	37.6	—	140,000[a]	176	[87]
Ni/CeO_2-NR (nanorods)	—	64	—	40,000[a]	121	[58]
Ni/CeO_2-NR (nanorods)	9.87	139	7.13	28,800	286	[85]

[a] WHSV in mL g^{-1} h^{-1}.

Table 7
CO conversion and specific activity values of CeO_2-comm, Ni/CeO_2-comm, CeO_2 TR, and Ni/CeO_2 TR samples at 100 °C. Reaction conditions: 2000 ppm CO, 1 vol% O_2, GHSV = 60,000 h^{-1}.

Sample	CO Conversion (%)	Specific activity			
		r_m (nmol g^{-1} s^{-1})	r_s (nmol m^{-2} s^{-1})	$r_{s,Ni}$ (nmol m_{Ni}^{-2} s^{-1})	STY (s^{-1})
CeO_2-comm	—	—	—	—	—
Ni/CeO_2-comm	0.52	18	5.49	0.65	$3.16 \cdot 10^{-4}$
CeO_2 TR	0.67	23	0.20	—	—
Ni/CeO_2 TR	15.2	518	6.10	21.59	$1.06 \cdot 10^{-2}$

In more detail, CO oxidation over ceria-based materials follows a Mars-van Krevelen, redox-type mechanism, involving alternating reduction/oxidation steps towards the formation of surface oxygen vacancies, their subsequent refill by gas phase oxygen, and the regeneration of metal active species in consecutive catalytic cycles [42,88,89]. In view of this fact, the pivotal role of the support's redox properties and its interaction with the nickel species is revealed. In particular, the enhanced oxygen exchange kinetics and reducibility of ceria facilitates the formation of active oxygen species, whereas the nickel-ceria synergistic interactions could be accounted for the facilitation of ceria capping oxygen reduction.

In light of the above discussion, Fig. 10 depicts the straightforward relationships revealed among the relative abundance of oxygen vacancies and the concentration of partially reduced cerium species (Ce^{3+}) with the CO specific consumption rate at 100 °C for the CO oxidation reaction and CO_2 consumption rate at 300 °C for the CO_2 hydrogenation

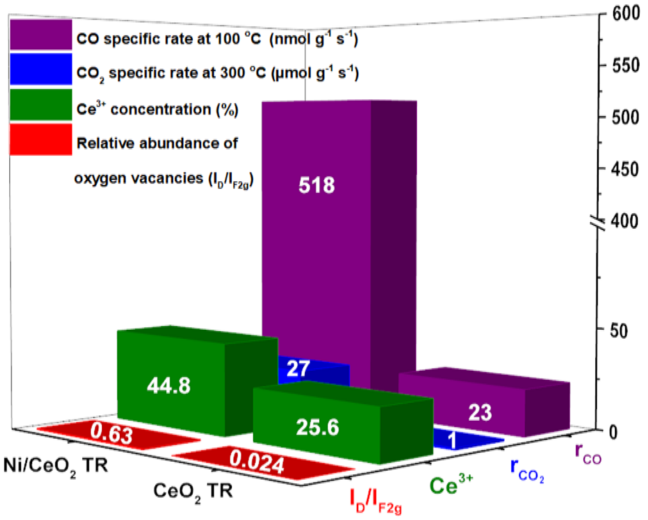

Fig. 10. Relationship among the CO consumption rate at 100 °C (CO oxidation reaction) and the CO_2 consumption rate at 300 °C (CO_2 hydrogenation reaction), with the relative abundance of oxygen vacancies and Ce^{3+} concentration for the CeO_2 TR and Ni/CeO_2 TR samples.

reaction, for bare CeO_2 TR and Ni/CeO_2 TR. The present results clearly demonstrate the fundamental role of ceria structure towards the determination of the relative abundance of structural defects/oxygen vacancies and Ce^{3+} species, which are crucial for both oxidation and reduction reactions.

In view of the above aspects, there is plenty of room towards the fine-tuning of 2D-based catalytic materials via the use of advanced synthesis and promotional routes, which could lead to highly-active and cost-efficient composites for various energy and environmental applications [90,91].

4. Conclusions

In the present work, thin-layered ceria nanoparticles of triangular-like morphology (TR) was synthesized through a simple solvothermal method and used as support for the nickel oxide phase. The as-prepared ceria and nickel-ceria samples, as well as the equivalent commercial oxides, were catalytically assessed in both hydrogenation and oxidation reactions, i.e., CO_2 methanation and CO oxidation. According to the characterization results, the Ni/CeO_2 TR catalyst exhibits enhanced reducibility with abundant structural defects and oxygen vacancies originating from the improved structural characteristics of ceria triangles. Ni/CeO_2 TR exhibits a CO_2 conversion value of 75 % and full methane selectivity at 380 °C while it also shows excellent CO oxidation performance, achieving full conversion at 280 °C. On the contrary, the corresponding commercial Ni/CeO_2-comm sample offers a much lower catalytic performance, revealing the significance of the ceria morphology in the overall catalytic behavior. The present findings clearly demonstrate that the employment of simple synthetic procedures, such as the solvothermal method, can lead to the development of innovative ceria structures with abundance on structural defects and oxygen vacancies, that can act as supporting carriers for transition metal active phases, leading to cost efficient and highly active materials for energy and environmental applications.

CRediT authorship contribution statement

Vassilios D. Binas: Methodology, Formal analysis, Conceptualization. **George E. Marnellos:** Writing – review & editing, Resources, Funding acquisition. **Michalis Konsolakis:** Writing – review & editing, Supervision, Resources, Methodology, Funding acquisition, Conceptualization. **Maria Lykaki:** Writing – review & editing, Writing – original draft, Methodology, Investigation, Formal analysis. **Sofia Stefa:** Writing – review & editing, Writing – original draft, Methodology, Investigation, Formal analysis. **Maria Zografaki:** Investigation. **Georgios Varvoutis:** Investigation.

Declaration of Competing Interest

The authors declare that they have no known competing financial interests or personal relationships that could have appeared to influence the work reported in this paper.

Acknowledgements

The authors would like to acknowledge funding by the European Union NextGenerationEU under the call RESEARCH – CREATE – INNOVATE 16971 Recovery and Resilience Facility (Project code: TAEDK-06169, NANOLEFINS), as well as funding received from the European Union under grant agreement No 101099717–ECOLEFINS project. Views and opinions expressed are, however, those of the author (s) only and do not necessarily reflect those of the European Union or European Innovation Council and SMEs Executive Agency (EISMEA) granting authority. Neither the European Union nor the granting authority can be held responsible for them.

Data availability

Data will be made available on request.

References

[1] M. Konsolakis, The role of Copper–Ceria interactions in catalysis science: Recent theoretical and experimental advances, Appl. Catal. B Environ. 198 (2016) 49–66, https://doi.org/10.1016/j.apcatb.2016.05.037.

[2] K. Chang, H. Zhang, M. Cheng, Q. Lu, Application of ceria in CO_2 conversion catalysis, ACS Catal. 10 (2020) 613–631, https://doi.org/10.1021/acscatal.9b03935.

[3] S. Sultana, S. Mansingh, K.M. Parida, Crystal facet and surface defect engineered low dimensional CeO_2 (0D, 1D, 2D) based photocatalytic materials towards energy generation and pollution abatement, Mater. Adv. 2 (2021) 6942–6983, https://doi.org/10.1039/D1MA00539A.

[4] J. Di, J. Xiong, H. Li, Z. Liu, Ultrathin 2D photocatalysts: electronic-structure tailoring, hybridization, and applications, Adv. Mater. 30 (2018) 1704548, https://doi.org/10.1002/adma.201704548.

[5] Z. Bian, Y.M. Chan, Y. Yu, S. Kawi, Morphology dependence of catalytic properties of Ni/CeO_2 for CO_2 methanation: a kinetic and mechanism study, Catal. Today 347 (2020) 31–38, https://doi.org/10.1016/j.cattod.2018.04.067.

[6] M. Lykaki, E. Pachatouridou, S.A.C. Carabineiro, E. Iliopoulou, C. Andriopoulou, N. Kallithrakas-Kontos, S. Boghosian, M. Konsolakis, Ceria nanoparticles shape effects on the structural defects and surface chemistry: Implications in CO oxidation by Cu/CeO_2 catalysts, Appl. Catal. B Environ. 230 (2018) 18–28, https://doi.org/10.1016/j.apcatb.2018.02.035.

[7] M. Tana, J. Zhang, H. Li, Y. Li, W. Shen, Morphology-dependent redox and catalytic properties of CeO2 nanostructures: Nanowires, nanorods and nanoparticles, Catal. Today 148 (2009) 179–183, https://doi.org/10.1016/j.cattod.2009.02.016.

[8] A.P.B. dos Santos, T.C.M. Dantas, J.A.P. Costa, L.D. Souza, J.M. Soares, V.P. S. Caldeira, A.S. Araújo, A.G.D. Santos, Formation of CeO_2 nanotubes through different conditions of hydrothermal synthesis, Surf. Interfaces 21 (2020) 100746, https://doi.org/10.1016/j.surfin.2020.100746.

[9] X. Yang, X. Gao, Y. Gan, C. Gao, X. Zhang, K. Ting, B.M. Wu, Z. Gou, Facile synthesis of octacalcium phosphate nanobelts: growth mechanism and surface adsorption properties, J. Phys. Chem. C 114 (2010) 6265–6271, https://doi.org/10.1021/jp911576f.

[10] Y. Chen, C. Qiu, C. Chen, X. Fan, S. Xu, W. Guo, Z. Wang, Facile synthesis of ceria nanospheres by Ce(OH)CO_3 precursors, Mater. Lett. 122 (2014) 90–93, https://doi.org/10.1016/j.matlet.2014.01.178.

[11] J. Gong, F. Meng, X. Yang, Z. Fan, H. Li, Controlled hydrothermal synthesis of triangular CeO_2 nanosheets and their formation mechanism and optical properties, J. Alloy. Compd. 689 (2016) 606–616, https://doi.org/10.1016/j.jallcom.2016.08.030.

[12] Y. Huang, B. Long, M. Tang, Z. Rui, M.-S. Balogun, Y. Tong, H. Ji, Bifunctional catalytic material: An ultrastable and high-performance surface defect CeO_2 nanosheets for formaldehyde thermal oxidation and photocatalytic oxidation, Appl. Catal. B Environ. 181 (2016) 779–787, https://doi.org/10.1016/j.apcatb.2015.08.047.

[13] F. Meng, J. Gong, Z. Fan, H. Li, J. Yuan, Hydrothermal synthesis and mechanism of triangular prism-like monocrystalline CeO_2 nanotubes via a facile template-free

hydrothermal route, Ceram. Int. 42 (2016) 4700–4708, https://doi.org/10.1016/j.ceramint.2015.11.123.

[14] D. Wang, Y. Kang, V. Doan-Nguyen, J. Chen, R. Küngas, N.L. Wieder, K. Bakhmutsky, R.J. Gorte, C.B. Murray, Synthesis and oxygen storage capacity of two-dimensional ceria nanocrystals, Angew. Chem. Int. Ed. 50 (2011) 4378–4381, https://doi.org/10.1002/anie.201101043.

[15] T. Yu, B. Lim, Y. Xia, Aqueous-phase synthesis of single-crystal ceria nanosheets, Angew. Chem. Int. Ed. 49 (2010) 4484–4487, https://doi.org/10.1002/anie.201001521.

[16] M. Konsolakis, M. Lykaki, Facet-dependent reactivity of ceria nanoparticles exemplified by CeO_2-based transition metal catalysts: a critical review, Catalysts 11 (2021) 452, https://doi.org/10.3390/catal11040452.

[17] M. Konsolakis, M. Lykaki, Recent advances on the rational design of non-precious metal oxide catalysts exemplified by CuO_x/CeO_2 binary system: implications of size, shape and electronic effects on intrinsic reactivity and metal-support interactions, Catalysts 10 (2020) 160, https://doi.org/10.3390/catal10020160.

[18] M. Lykaki, E. Mandela, G. Varvoutis, A. Lampropoulos, G.E. Marnellos, M. Konsolakis, State-of-the-art thermocatalytic systems for CH_4 and CO production via CO_2 hydrogenation: critical comparison, mechanistic considerations and structure-performance insights, Discov. Chem. Eng. 4 (2024) 11, https://doi.org/10.1007/s43938-024-00048-7.

[19] G. Varvoutis, M. Lykaki, G.E. Marnellos, M. Konsolakis, Recent advances on fine-tuning engineering strategies of CeO_2-based nanostructured catalysts exemplified by CO_2 hydrogenation processes, Catalysts 13 (2023) 275, https://doi.org/10.3390/catal13020275.

[20] L. Atzori, M.G. Cutrufello, D. Meloni, C. Cannas, D. Gazzoli, R. Monaci, M.F. Sini, E. Rombi, Highly active NiO-CeO_2 catalysts for synthetic natural gas production by CO_2 methanation, Catal. Today 299 (2018) 183–192, https://doi.org/10.1016/j.cattod.2017.05.065.

[21] T. Jomjaree, P. Sintuya, A. Srifa, W. Koo-amornpattana, S. Kiatphuengporn, S. Assabumrungrat, M. Sudoh, R. Watanabe, C. Fukuhara, S. Ratchahat, Catalytic performance of Ni catalysts supported on CeO_2 with different morphologies for low-temperature CO_2 methanation, Catal. Today 375 (2021) 234–244, https://doi.org/10.1016/j.cattod.2020.08.010.

[22] N. Rui, X. Zhang, Feng Zhang, Z. Liu, X. Cao, Z. Xie, R. Zou, S.D. Senanayake, Y. Yang, J.A. Rodriguez, C.-J. Liu, Highly active Ni/CeO_2 catalyst for CO_2 methanation: Preparation and characterization, Appl. Catal. B Environ. 282 (2021) 119581, https://doi.org/10.1016/j.apcatb.2020.119581.

[23] R.-P. Ye, Q. Li, W. Gong, T. Wang, J.J. Razink, L. Lin, Y.-Y. Qin, Z. Zhou, H. Adidharma, J. Tang, A.G. Russell, M. Fan, Y.-G. Yao, High-performance of nanostructured Ni/CeO_2 catalyst on CO_2 methanation, Appl. Catal. B Environ. 268 (2020) 118474, https://doi.org/10.1016/j.apcatb.2019.118474.

[24] R. Khobragade, M. Roškarič, G. Žerjav, M. Košiček, J. Zavašnik, N. Van de Velde, I. Jerman, N.N. Tušar, A. Pintar, Exploring the effect of morphology and surface properties of nanoshaped Pd/CeO_2 catalysts on CO_2 hydrogenation to methanol, Appl. Catal. A Gen. 627 (2021) 118394, https://doi.org/10.1016/j.apcata.2021.118394.

[25] Y. Du, C. Qin, Y. Xu, D. Xu, J. Bai, G. Ma, M. Ding, Ni nanoparticles dispersed on oxygen vacancies-rich CeO_2 nanoplates for enhanced low-temperature CO_2 methanation performance, Chem. Eng. J. 418 (2021) 129402, https://doi.org/10.1016/j.cej.2021.129402.

[26] L. Fan, J. Zhang, K. Ma, Y. Zhang, Y.-M. Hu, L. Kong, A. Jia, Z. Zhang, W. Huang, J.-Q. Lu, Ceria morphology-dependent Pd-CeO_2 interaction and catalysis in CO_2 hydrogenation into formate, J. Catal. 397 (2021) 116–127, https://doi.org/10.1016/j.jcat.2021.03.025.

[27] F. Jiang, S. Wang, B. Liu, J. Liu, L. Wang, Y. Xiao, Y. Xu, X. Liu, Insights into the influence of CeO_2 crystal facet on CO_2 hydrogenation to methanol over Pd/CeO_2 catalysts, ACS Catal. 10 (2020) 11493–11509, https://doi.org/10.1021/acscatal.0c03324.

[28] Z.-A. Qiao, Z. Wu, S. Dai, Shape-controlled ceria-based nanostructures for catalysis applications, ChemSusChem 6 (2013) 1821–1833, https://doi.org/10.1002/cssc.201300428.

[29] N. Ta, J. Liu, W. Shen, Tuning the shape of ceria nanomaterials for catalytic applications, Chin. J. Catal. 34 (2013) 838–850, https://doi.org/10.1016/S1872-2067(12)60573-7.

[30] G. Varvoutis, M. Lykaki, S. Stefa, E. Papista, S.A.C. Carabineiro, G.E. Marnellos, M. Konsolakis, Remarkable efficiency of Ni supported on hydrothermally synthesized CeO_2 nanorods for low-temperature CO_2 hydrogenation to methane, Catal. Commun. 142 (2020) 106036, https://doi.org/10.1016/j.catcom.2020.106036.

[31] B. Yang, Y. Wang, L. Li, B. Gao, L. Zhang, L. Guo, Probing the morphological effects of ReO_x/CeO_2 catalysts on the CO_2 hydrogenation reaction, Catal. Sci. Technol. 12 (2022) 1159–1172, https://doi.org/10.1039/d1cy02096j.

[32] S. Lin, Z. Li, M. Li, Tailoring metal-support interactions via tuning CeO_2 particle size for enhancing CO_2 methanation activity over Ni/CeO_2 catalysts, Fuel 333 (2023) 126369, https://doi.org/10.1016/j.fuel.2022.126369.

[33] N.M. Martin, F. Hemmingsson, A. Schaefer, M. Ek, L.R. Merte, U. Hejral, J. Gustafson, M. Skoglundh, A.-C. Dippel, O. Gutowski, M. Bauer, P.-A. Carlsson, Structure-function relationship for CO_2 methanation over ceria supported Rh and Ni catalysts under atmospheric pressure conditions, Catal. Sci. Technol. 9 (2019) 1644–1653, https://doi.org/10.1039/c8cy02097c.

[34] S. Lin, Z. Hao, J. Shen, X. Chang, S. Huang, M. Li, X. Ma, Enhancing the CO_2 methanation activity of Ni/CeO_2 via activation treatment-determined metal-support interaction, J. Energy Chem. 59 (2021) 334–342, https://doi.org/10.1016/j.jechem.2020.11.011.

[35] G.I. Siakavelas, N.D. Charisiou, S. AlKhoori, A.A. AlKhoori, V. Sebastian, S. J. Hinder, M.A. Baker, I.V. Yentekakis, K. Polychronopoulou, M.A. Goula, Highly selective and stable nickel catalysts supported on ceria promoted with Sm_2O_3, Pr_2O_3 and MgO for the CO_2 methanation reaction, Appl. Catal. B Environ. 282 (2021) 119562, https://doi.org/10.1016/j.apcatb.2020.119562.

[36] J. Li, Y. Lin, X. Pan, D. Miao, D. Ding, Y. Cui, J. Dong, X. Bao, Enhanced CO_2 methanation activity of Ni/anatase catalyst by tuning strong metal-support interactions, ACS Catal. 9 (2019) 6342–6348, https://doi.org/10.1021/acscatal.9b00401.

[37] W.J. Lee, C. Li, H. Prajitno, J. Yoo, J. Patel, Y. Yang, S. Limet, Recent trend in thermal catalytic low temperature CO_2 methanation: A critical review, Catal. Today 368 (2021) 2–19, https://doi.org/10.1016/j.cattod.2020.02.017.

[38] A.D.N. Kamkeng, M. Wang, J. Hu, W. Du, F. Qian, Transformation technologies for CO_2 utilisation: Current status, challenges and future prospects, Chem. Eng. J. 409 (2021) 128138, https://doi.org/10.1016/j.cej.2020.128138.

[39] T.A. Atsbha, T. Yoon, P. Seongho, C.-J. Lee, A review on the catalytic conversion of CO_2 using H_2 for synthesis of CO, methanol, and hydrocarbons, J. CO2 Util. 44 (2021) 101413, https://doi.org/10.1016/j.jcou.2020.101413.

[40] N. Ali, M. Bilal, M.S. Nazir, A. Khan, F. Ali, H.M.N. Iqbal, Thermochemical and electrochemical aspects of carbon dioxide methanation: A sustainable approach to generate fuel via waste to energy theme, Sci. Total Environ. 712 (2020) 136482, https://doi.org/10.1016/j.scitotenv.2019.136482.

[41] S. Royer, D. Duprez, Catalytic oxidation of carbon monoxide over transition metal oxides, ChemCatChem 3 (2011) 24–65, https://doi.org/10.1002/cctc.201000378.

[42] K. Polychronopoulou, A.A. AlKhoori, A.M. Efstathiou, M.A. Jaoude, C. M. Damaskinos, M.A. Baker, A. Almutawa, D.H. Anjum, M.A. Vasiliades, A. Belabbes, L.F. Vega, A.F. Zedan, S.J. Hinder, Design aspects of doped CeO_2 for low-temperature catalytic CO oxidation: transient kinetics and DFT approach, ACS Appl. Mater. Interfaces 13 (2021) 22391–22415, https://doi.org/10.1021/acsami.1c02934.

[43] M. Lykaki, S. Stefa, S.A.C. Carabineiro, P.K. Pandis, V.N. Stathopoulos, M. Konsolakis, Facet-dependent reactivity of Fe_2O_3/CeO_2 nanocomposites: effect of ceria morphology on CO oxidation, Catalysts 9 (2019) 371, https://doi.org/10.3390/catal9040371.

[44] M. Zografaki, S. Stefa, I. Vamvasakis, G.S. Armatas, A.G. Chaidali, I.N. Lykakis, V. Binas, Triangle CeO_2/g-C_3N_4 heterojunctions: Enhanced light-driven photocatalytic degradation of methylparaben, J. Photochem. Photobiol. A Chem. 458 (2025) 115976, https://doi.org/10.1016/j.jphotochem.2024.115976.

[45] G. Varvoutis, S.A. Karakoulia, M. Lykaki, S. Stefa, V. Binas, G.E. Marnellos, M. Konsolakis, Support-induced modifications on the CO2 hydrogenation performance of Ni/CeO_2: The effect of ZnO doping on CeO_2 nanorods, J. CO2 Util. 61 (2022) 102057, https://doi.org/10.1016/j.jcou.2022.102057.

[46] G. Varvoutis, M. Lykaki, S. Stefa, V. Binas, G.E. Marnellos, M. Konsolakis, Deciphering the role of Ni particle size and nickel-ceria interfacial perimeter in the low-temperature CO_2 methanation reaction over remarkably active Ni/CeO_2 nanorods, Appl. Catal. B Environ. 297 (2021) 120401, https://doi.org/10.1016/j.apcatb.2021.120401.

[47] S.T. Hossain, E. Azeeva, K. Zhang, E.T. Zell, D.T. Bernard, S. Balaz, R. Wang, A comparative study of CO oxidation over Cu-O-Ce solid solutions and CuO/CeO_2 nanorods catalysts, Appl. Surf. Sci. 455 (2018) 132–143, https://doi.org/10.1016/j.apsusc.2018.05.101.

[48] J. Ma, G. Jin, J. Gao, Y. Li, L. Dong, M. Huang, Q. Huang, B. Li, Catalytic effect of two-phase intergrowth and coexistence CuO–CeO_2, J. Mater. Chem. A 3 (2015) 24358–24370, https://doi.org/10.1039/C5TA06435J.

[49] L. Qi, Q. Yu, Y. Dai, C. Tang, L. Liu, H. Zhang, F. Gao, L. Dong, Y. Chen, Influence of cerium precursors on the structure and reducibility of mesoporous CuO-CeO_2 catalysts for CO oxidation, Appl. Catal. B Environ. 119–120 (2012) 308–320, https://doi.org/10.1016/j.apcatb.2012.02.029.

[50] T.R. Sahoo, M. Armandi, R. Arletti, M. Piumetti, S. Bensaid, M. Manzoli, S. R. Panda, B. Bonelli, Pure and Fe-doped CeO_2 nanoparticles obtained by microwave assisted combustion synthesis: Physico-chemical properties ruling their catalytic activity towards CO oxidation and soot combustion, Appl. Catal. B Environ. 211 (2017) 31–45, https://doi.org/10.1016/j.apcatb.2017.04.032.

[51] P. Sudarsanam, B. Hillary, M.H. Amin, N. Rockstroh, U. Bentrup, A. Brückner, S. K. Bhargava, Heterostructured copper–ceria and iron–ceria nanorods: role of morphology, redox, and acid properties in catalytic diesel soot combustion, Langmuir 34 (2018) 2663–2673, https://doi.org/10.1021/acs.langmuir.7b03998.

[52] V. Golovanova, M.C. Spadaro, J. Arbiol, V. Golovanov, T.T. Rantala, T. Andreu, J. R. Morante, Effects of solar irradiation on thermally driven CO_2 methanation using Ni/CeO_2–based catalyst, Appl. Catal. B Environ. 291 (2021) 120038, https://doi.org/10.1016/j.apcatb.2021.120038.

[53] M. Konsolakis, M. Lykaki, S. Stefa, S.A.C. Carabineiro, G. Varvoutis, E. Papista, G. E. Marnellos, CO_2 Hydrogenation over nanoceria-supported transition metal catalysts: role of ceria morphology (nanorods versus nanocubes) and active phase nature (Co versus Cu), Nanomaterials 9 (2019) 1739, https://doi.org/10.3390/nano9121739.

[54] N. Wang, W. Qian, W. Chu, F. Wei, Crystal-plane effect of nanoscale CeO_2 on the catalytic performance of Ni/CeO_2 catalysts for methane dry reforming, Catal. Sci. Technol. 6 (2016) 3594–3605, https://doi.org/10.1039/C5CY01790D.

[55] S. Liu, X. Liao, Q. Zhang, Y. Zhang, H. Wang, Y. Zhao, Crystal-plane and shape influences of nanoscale CeO_2 on the activity of Ni/CeO_2 catalysts for maleic anhydride hydrogenation, Nanomaterials 12 (2022) 762, https://doi.org/10.3390/nano12050762.

[56] Z. Ren, F. Peng, B. Chen, D. Mei, J. Li, A combined experimental and computational study of water-gas shift reaction over rod-shaped $Ce_{0.75}M_{0.25}O_2$ (M = Ti, Zr, and

Mn) supported Cu catalysts, Int. J. Hydrogen Energy 42 (51) (2017) 30086–30097, https://doi.org/10.1016/j.ijhydene.2017.10.047.

[57] Z. Hu, S. Qiu, Y. You, Y. Guo, Y. Guo, L. Wang, W. Zhan, G. Lu, Hydrothermal synthesis of NiCeO$_x$ nanosheets and its application to the total oxidation of propane, Appl. Catal. B Environ. 225 (2018) 110–120, https://doi.org/10.1016/j.apcatb.2017.08.068.

[58] W. Zou, C. Ge, M. Lu, S. Wu, Y. Wang, J. Sun, Y. Pu, C. Tang, F. Gao, L. Dong, Engineering the NiO/CeO$_2$ interface to enhance the catalytic performance for CO oxidation, RSC Adv. 5 (2015) 98335–98343, https://doi.org/10.1039/C5RA20466F.

[59] I. Iglesias, G. Baronetti, F. Mariño, Ceria and Ce$_{0.95}$ M$_{0.05}$O$_{2-\delta}$ mixed oxides (M = La, Pr, Zr): Vacancies and reducibility study, Solid State Ion. 309 (2017) 123–129, https://doi.org/10.1016/j.ssi.2017.07.008.

[60] P. Zhao, F. Qin, Z. Huang, C. Sun, W. Shen, H. Xu, Morphology-dependent oxygen vacancies and synergistic effects of Ni/CeO$_2$ catalysts for N$_2$O decomposition, Catal. Sci. Technol. 8 (2018) 276–288, https://doi.org/10.1039/c7cy02301d.

[61] A. Pfau, K.D. Schierbaum, The electronic structure of stoichiometric and reduced CeO$_2$ surfaces: an XPS, UPS and HREELS study, Surf. Sci. 321 (1994) 71–80, https://doi.org/10.1016/0039-6028(94)90027-2.

[62] M. Li, A.C. van Veen, Tuning the catalytic performance of Ni-catalysed dry reforming of methane and carbon deposition via Ni-CeO$_{2\text{-x}}$ interaction, Appl. Catal. B Environ. 237 (2018) 641–648, https://doi.org/10.1016/j.apcatb.2018.06.032.

[63] I. Chakraborty, D. Ghosh, S.M. Sathe, B.K. Dubey, D. Pradhan, M.M. Ghangrekar, Investigating the efficacy of CeO$_2$ multi-layered triangular nanosheets for augmenting cathodic hydrogen peroxide production in microbial fuel cell, Electrochim. Acta 398 (2021) 139341, https://doi.org/10.1016/j.electacta.2021.139341.

[64] M. Lykaki, S. Stefa, G. Varvoutis, V.D. Binas, G.E. Marnellos, M. Konsolakis, Comparative assessment of first-row 3d transition metals (Ti-Zn) supported on CeO$_2$ nanorods for CO$_2$ hydrogenation, Catalysts 14 (2024) 611, https://doi.org/10.3390/catal14090611.

[65] Y. Lee, G. He, A.J. Akey, R. Si, M. Flytzani-Stephanopoulos, I.P. Herman, Raman analysis of mode softening in nanoparticle CeO$_{2-\delta}$ and Au-CeO$_{2-\delta}$ during CO oxidation, J. Am. Chem. Soc. 133 (2011) 12952–12955, https://doi.org/10.1021/ja204479j.

[66] L. Cardenas, C. Molinet-Chinaglia, S. Loridant, Unraveling Ce^{3+} detection at the surface of ceria nanopowders by UPS analysis, Phys. Chem. Chem. Phys. 24 (2022) 22815–22822, https://doi.org/10.1039/d2cp02736d.

[67] M. Lykaki, E. Pachatouridou, E. Iliopoulou, S.A.C. Carabineiro, M. Konsolakis, Impact of the synthesis parameters on the solid state properties and the CO oxidation performance of ceria nanoparticles, RSC Adv. 7 (2017) 6160–6169, https://doi.org/10.1039/C6RA26712B.

[68] P. Maitarad, J. Han, D. Zhang, L. Shi, S. Namuangruk, T. Rungrotmongkol, Structure–activity relationships of NiO on CeO$_2$ nanorods for the selective catalytic reduction of NO with NH$_3$: experimental and DFT studies, J. Phys. Chem. C 118 (2014) 9612–9620, https://doi.org/10.1021/jp5024845.

[69] E. Marconi, S. Tuti, I. Luisetto, Structure-sensitivity of CO$_2$ methanation over nanostructured Ni supported on CeO$_2$ nanorods, Catalysts 9 (2019) 375, https://doi.org/10.3390/catal9040375.

[70] T. Nguyen, B.L. Do, P.A. Nguyen, T.T. Van Nguyen, C.A. Ha, T.C. Hoang, C.L. Luu, Nickel/ceria nanorod catalysts for the synthesis of substitute natural gas from CO$_2$: Effect of active phase loading and synthesis condition, J. Sci. Adv. Mater. Devices 9 (2024) 100752, https://doi.org/10.1016/j.jsamd.2024.100752.

[71] G. Pantaleo, V.La Parola, F. Deganello, R.K. Singha, R. Bal, A.M. Venezia, Ni/CeO$_2$ catalysts for methane partial oxidation: Synthesis driven structural and catalytic effects, Appl. Catal. B Environ. 189 (2016) 233–241, https://doi.org/10.1016/j.apcatb.2016.02.064.

[72] A. Quindimil, U. De-La-Torre, B. Pereda-Ayo, A. Davó-Quiñonero, E. Bailón-García, D. Lozano-Castelló, J.A. González-Marcos, A. Bueno-López, J.R. González-Velasco, Effect of metal loading on the CO$_2$ methanation: A comparison between alumina supported Ni and Ru catalysts, Catal. Today 356 (2020) 419–432, https://doi.org/10.1016/j.cattod.2019.06.027.

[73] J. Lin, C. Ma, Q. Wang, Y. Xu, G. Ma, J. Wang, H. Wang, C. Dong, C. Zhang, M. Ding, Enhanced low-temperature performance of CO$_2$ methanation over mesoporous Ni/Al$_2$O$_3$-ZrO$_2$ catalysts, Appl. Catal. B Environ. 243 (2019) 262–272, https://doi.org/10.1016/j.apcatb.2018.10.059.

[74] V. Shanmugam, R.A. Mensah, K. Babu, S. Gawusu, A. Chanda, Y. Tu, R.E. Neisiany, M. Försth, G. Sas, O. Das, A review of the synthesis, properties, and applications of 2D materials, Part. Part. Syst. Charact. 39 (2022) 2200031, https://doi.org/10.1002/ppsc.202200031.

[75] N. Baig, Two-dimensional nanomaterials: A critical review of recent progress, properties, applications, and future directions, Compos. Part A Appl. Sci. Manuf. 165 (2023) 107362, https://doi.org/10.1016/j.compositesa.2022.107362.

[76] Y. Xie, J. Chen, X. Wu, J. Wen, R. Zhao, Z. Li, G. Tian, Q. Zhang, P. Ning, J. Hao, Frustrated Lewis Pairs boosting low-temperature CO$_2$ methanation performance over Ni/CeO$_2$ nanocatalysts, ACS Catal. 12 (2022) 10587–10602, https://doi.org/10.1021/acscatal.2c02535.

[77] Y. Bian, C. Xu, X. Wen, L. Xu, Y. Cui, S. Wang, C. Wu, J. Qiu, G. Cheng, M. Chen, CO$_2$ methanation over the Ni-based catalysts supported on nano-CeO$_2$ with varied morphologies, Fuel 331 (2023) 125755, https://doi.org/10.1016/j.fuel.2022.125755.

[78] N. Hashimoto, K. Mori, K. Asahara, S. Shibata, H. Jida, Y. Kuwahara, H. Yamashita, How the morphology of NiO$_x$-decorated CeO$_2$ nanostructures affects catalytic properties in CO$_2$ methanation, Langmuir 37 (2021) 5376–5384, https://doi.org/10.1021/acs.langmuir.1c00546.

[79] Y. Zhang, T. Zhang, F. Wang, Q. Zhu, Q. Liu, Ni/CeO$_2$ catalysts for low-temperature CO$_2$ methanation: Identifying effect of support morphology and oxygen vacancy, Greenh. Gases Sci. Technol. 11 (2021) 1222–1233, https://doi.org/10.1002/ghg.2121.

[80] X. Chen, R. Ye, C. Sun, C. Jin, Y. Wang, H. Arandiyan, K.H. Lim, G. Song, F. Hu, C. Li, Z.-H. Lu, G. Feng, R. Zhang, S. Kawi, Optimizing low-temperature CO$_2$ methanation through frustrated Lewis pairs on Ni/CeO$_2$ catalysts, Chem. Eng. J. 484 (2024) 149471, https://doi.org/10.1016/j.cej.2024.149471.

[81] M.I. Alam, R. Cheula, G. Moroni, L. Nardi, M. Maestri, Mechanistic and multiscale aspects of thermo-catalytic CO$_2$ conversion to C$_1$ products, Catal. Sci. Technol. 11 (2021) 6601–6629, https://doi.org/10.1039/D1CY00922B.

[82] Y. Xie, J. Wen, Z. Li, J. Chen, Q. Zhang, P. Ning, Y. Chen, J. Hao, Progress in reaction mechanisms and catalyst development of ceria-based catalysts for low-temperature CO$_2$ methanation, Green Chem. 25 (2023) 130–152, https://doi.org/10.1039/D2GC03512J.

[83] S. Musab Ahmed, J. Ren, I. Ullah, H. Lou, N. Xu, Z. Abbasi, Z. Wang, Ni-based catalysts for CO$_2$ methanation: exploring the support role in structure-activity relationships, ChemSusChem 17 (2024) e202400310, https://doi.org/10.1002/cssc.202400310.

[84] M. Boaro, S. Colussi, A. Trovarelli, Ceria-based materials in hydrogenation and reforming reactions for CO$_2$ valorization, Front. Chem. 7 (2019) 28, https://doi.org/10.3389/fchem.2019.00028.

[85] D. Jampaiah, P. Venkataswamy, V.E. Coyle, B.M. Reddy, S.K. Bhargava, Low-temperature CO oxidation over manganese, cobalt, and nickel doped CeO$_2$ nanorods, RSC Adv. 6 (2016) 80541–80548, https://doi.org/10.1039/c6ra13577c.

[86] J. Hu, F. Wei, X. Hu, J. Xu, W. Deng, Synthesis of CuO-loaded ceria hollow spheres for catalytic CO oxidation, ChemistrySelect 7 (2022) e202103476, https://doi.org/10.1002/slct.202103476.

[87] S.A. Mock, S.E. Sharp, T.R. Stoner, M.J. Radetic, E.T. Zell, R. Wang, CeO$_2$ nanorods-supported transition metal catalysts for CO oxidation, J. Colloid Interface Sci. 466 (2016) 261–267, https://doi.org/10.1016/j.jcis.2015.12.026.

[88] W.-W. Wang, W.-Z. Yu, P.-P. Du, H. Xu, Z. Jin, R. Si, C. Ma, S. Shi, C.-J. Jia, C.-H. Yan, Crystal plane effect of ceria on supported copper oxide cluster catalyst for CO oxidation: Importance of metal–support interaction, ACS Catal. 7 (2017) 1313–1329, https://doi.org/10.1021/acscatal.6b03234.

[89] L. Wang, S. Deo, K. Dooley, M.J. Janik, R.M. Rioux, Influence of metal nuclearity and physicochemical properties of ceria on the oxidation of carbon monoxide, Chin. J. Catal. 41 (2020) 951–962, https://doi.org/10.1016/S1872-2067(20)63557-4.

[90] C. Wang, S. Guan, H. Zhang, R. Shen, H. Yuan, B. Li, Perspectives on two-dimensional ultra-thin materials in energy catalysis and storage, APL Mater. 11 (2023) 050902, https://doi.org/10.1063/5.0148143.

[91] Y. Wang, J. Mao, X. Meng, L. Yu, D. Deng, X. Bao, Catalysis with two-dimensional materials confining single atoms: concept, design, and applications, Chem. Rev. 119 (2019) 1806–1854, https://doi.org/10.1021/acs.chemrev.8b00501.